

**Figure 5.8.** Portrait diagram display of number of seasons for which the correlation of node frequency between NARR and GCM is significantly different from zero (at the 95% confidence level). Columns refer to the SOM size (4×3, 4×4, and 5×4) and spatial domain (large and small). Red squares mark models where all seasons have correlation significantly different from zero, while dark blue squares mark models where no season has a correlation significantly different from zero.

#### 5.4 Criteria for the selection of GCMs

In this section we identify a set of criteria for selecting an ensemble of GCMs whose climate projections will be used in our glacier and hydrologic modelling in the Columbia basin. The criteria are primarily derived from the evaluation of GCMs with a set of performance metrics as presented in the previous sections. We choose a methodology which rejects every GCM that does not satisfy a certain condition. Thus, the final ensemble consists of the GCMs that satisfy each of the following criteria:

1. GCM data for 20th and 21st century are fully accessible (archived at the LLNL) for the purpose of our model evaluation analysis, downscaling, and glacier and hydrologic modelling. The emphasis is on availability of daily GCM data because TreeGen downscaling and the hydrologic model operate on daily time scales.
2. A model's relative error for 1980–1999 annual cycle climatology calculated in Gleckler *et al.* (2008) is not greater than 0.5 for any considered climate variable over the full global domain (see Figure 3a in Gleckler *et al.*, 2008). In other words, models with relative errors larger than 50%

from the typical error (median of relative errors across the 22 GCMs) are excluded from the ensemble.

3. When ranked according to our set of statistical metrics (relative error, MCPI and MVI) the model is not in the bottom place for any climate variable and spatial domain (Figure 5.4). Thus, models that have at least one blue square in the portrait diagram in Figure 5.4 are excluded.
4. According to GCM evaluation with SOM, the model produces node frequencies that are significantly correlated to node frequencies from NARR for at least one season, over both the large and small domain, and all SOM sizes (Figure 5.8). In other words, models with no significant correlation for any season are excluded from the ensemble.

The results of our model selection are summarized in Box 5.1. The final ensemble consists of the following six models listed alphabetically:

1. CGCM3.1(T47)
2. CGCM3.1(T63)
3. CSIRO-Mk3.0
4. GFDL-CM2.0
5. MIROC3.2(hires)
6. ECHAM/MPI-OM.

Our aim is to use the 21st century climate projections from these six models, run under atmospheric greenhouse gas concentrations from three SRES scenarios: A2, A1B, and B1 (Alley et al., 2007). The summary of the three emission scenarios, adopted from Alley *et al.* (2007), is given in Box 5.2.



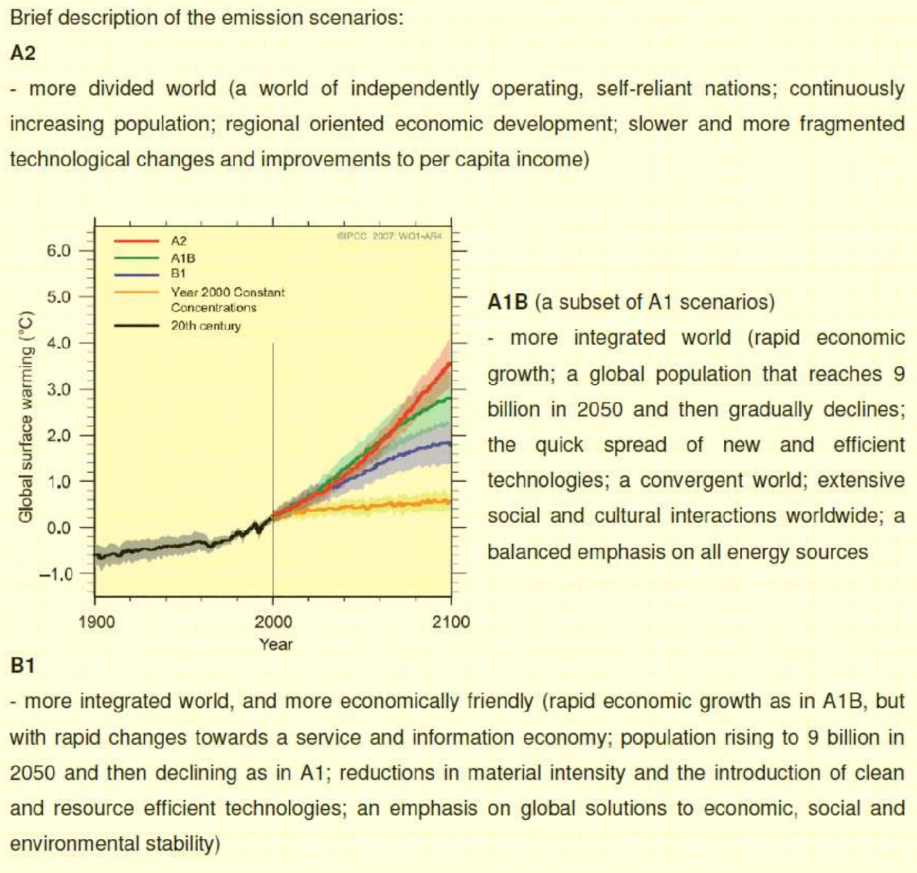
### Box 5.1. Selection of GCMs

GCM	Criterion			
	1	2	3	4
BCCR-BCM2.0	x	x	x	
<b>CGCM3.1(T47)</b>	x	x	x	
<b>CGCM3.1(T63)</b>	x	x	x	
<b>CSIRO-Mk3.0</b>	x	x	x	
CNRM-CM3	x	x	x	
ECHO-G		x	x	
<b>GFDL-CM2.0</b>	x	x	x	
GFDL-CM2.1		x	x	
GISS-AOM			x	
GISS-EH				
GISS-ER		x		x
FGOALS-g1.0				
INM-CM3.0				x
IPSL-CM4	x			
MIROC3.2(medres)	x	x	x	
<b>MIROC3.2(hires)</b>	x	x	x	
MRI-CGCM2.3.2	x			x
<b>ECHAM5/MPI-OM</b>	x	x	x	
CCSM3			x	
PCM	x			
UKMO-HadCM3		x	x	x
UKMO-HadGEM1		x	x	

GCMs checked with x satisfy the following criteria:

- 1) availability of required (daily) GCM data
- 2) good performance over the global domain according to the statistical metric calculated in Gleckler et al. (2008); *model simulation of mean annual cycle*
- 3) good performance over the large and small domain according to the set of statistical metrics; *model simulation of mean annual cycle and inter-annual variability*
- 4) good performance over the large and small domain according to the correlation of node frequencies in self-organizing maps; *model simulation of occurrences of daily synoptic patterns on seasonal basis*

**Box 5.2.** The emission scenarios (adopted from Alley *et al.*, 2007)



In order to explore the range of future climate projections represented by the six selected models for the BC Columbia Basin, we use the Regional Analysis Tool (RAT; PCIC, 2010).which provides analytical capabilities for GCM data, focusing on regional results. The tool includes data covering North America from GCM scenarios prepared for the IPCC Third Assessment and global data from more than 15 GCMs for the IPCC Fourth Assessment (AR4). Maps, plots and data can be produced with the RAT based on a custom region. These include plots of variable against variable (e.g., precipitation vs. temperature) scatter plots for each ensemble, and box plots of projected change by time slice including the 2020s (2011-2040), 2050s (2041-2070) and 2080s (2071-2100). Metadata are provided for all images, such as values of projected changes in climatic variables for each selected GCM. As a result of this analysis, in Figure 5.9 we plot the projected total changes in temperature and precipitation, according to all three emission scenarios, between two future periods: 2050s (2041–2070) and 2080s (2071–2100) and the reference period 1961–1990. The projected changes are plotted for two ensembles of models: the ensemble of all 22 GCMs from CMIP3 and the ensemble of six selected GCMs. As illustrated, the range of possible future

climates for Columbia Basin (warm-wet, warm-dry, cool-wet and cool-dry) projected from 22 GCMs is well represented by the ensemble of six selected models. We note that one model in our selected ensemble (MIROC3.2\_hires) does not have data available for the A2 emission scenario.

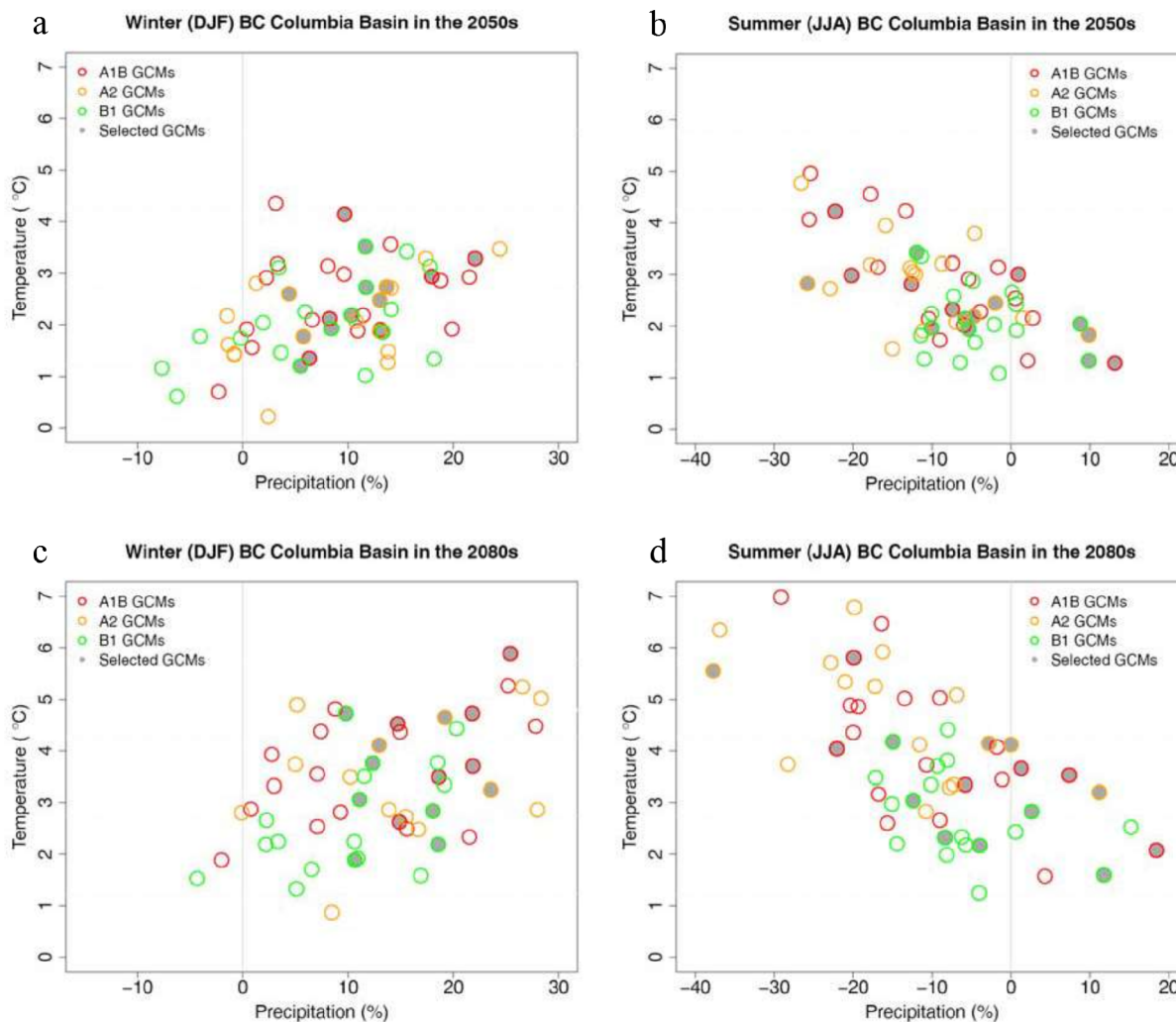


**Figure 5.9.** Projected total changes in temperature and precipitation between future period and the reference period (1961–1990), for all 22 GCMs and all three emission scenarios (A1B, A2, and B1). (a) Winter 2050s (2041–2070), (b) Summer 2050s, (c) Winter 2080s (2071–2100). (d) Summer 2080s. Projections from the selected six GCMs are represented by the filled circles.

## 5.5 Discussion and future directions




One important characteristic of a representative ensemble is that artificial coherencies between models that might contaminate the statistics (Leduc and Laprise, 2010) are kept small. However, several GCMs are known not to be totally independent, such as models from the same group that differ in their

resolution. In this study, we are constrained by the available models, especially by those with daily data, and we are trying to select a set of 5 or 6 models that are representative. Through our assessment of performance, we have selected two models from the same modelling centre that differ only in their resolution: CGCM3.1(T47) and CGCM3.1(T63). Table 5.4 summarizes the differences between consanguineous model pairs in the CMIP3 sample.

Selecting two models from the same modelling centre has the potential to weight results towards a given model. The CGCM3.1(T47) and T63 models were similar to each other when compared to the distribution of the root-square differences for all random pairs ( $\sim 10^{143}$ ). They were found to be more similar than MIROC(hires/T42) and MIROC(medres/T106), which also only differ in their resolution and less similar, in some regions of North America, than GFDL CM2.0 and GFDL CM2.1 which vary in their parameterization (Leduc and Laprise, 2010).

We have analyzed model performance based on model simulation of the mean annual cycle, inter-annual variability and simulation of occurrences of daily synoptic patterns on a seasonal basis. One outstanding test applied by several other studies (Mote and Salathé, 2009; Christensen *et al.*, 2010) includes comparing linear temperature trends from the historic model to observed records over a region. This comparison is seen as an indicator of the sensitivity to greenhouse gas forcing for a given GCM and of its ability to project changing climate into the future. In the case of dynamically modelling glacier change, selecting GCMs which evolved historically much like the observed climate might have eased the transition from simulated historical glacier conditions to future projections. However, selection of a representative observed dataset with which to compare trends remains a challenge. The NARR dataset which was used for much of this work spans only from 1980 to present, which is too short for trend detection studies and introducing additional longer term datasets would have complicated comparison of GCM performance across metrics. . This remains a possible addition for future work.

**Table 5.4.** A summary of differences between consanguineous model pairs in the CMIP3 selection adapted from Leduc and Laprise (2010).

<b>Pair</b>	<b>Model</b>	<b>Difference</b>
<b>I</b>	CGCM3: T47 & T63	Change of $\Delta_{xy}$
<b>II</b>	MIROC: T42 & T106	Change of $\Delta_{xy}$
<b>III</b>	CSIRO: 3.0 & 3.5	New version of the temporal scheme, ameliorations in runoff, river routing and coupling (surface fluxes)
<b>IV</b>	GFDL: CM2.0 & CM2.1	Equations discretization (advection, temporal scheme), parameters adjustment (gravity waves, divergence)
<b>V</b>	GISS: AOM & EH	Different atmospheric and  and land and surface schemes
<b>VI</b>	GISS: AOM & ER	Different atmospheric and  and land and surface schemes
<b>VII</b>	GISS: EH & ER	Same atmosphere and different 
<b>VIII</b>	HadCM3 & HadGEM1	Different models developed by the same institute.

## 6 Glacier response to future climate scenarios

### 6.1 20<sup>th</sup> century glacier evolution

As a necessary prelude to our simulations of projected 21<sup>st</sup> century glacier change, we simulated the evolution of glaciers in response to known climate change during the 20<sup>th</sup> century. These simulations provide a context for assessing the 21<sup>st</sup> century results and allow model results to be compared with published measurements of glacier change. There is some uncertainty in the early part of the simulation due to spin-up effects, but these appear to have damped out by the 1920s. Figure 6.1 gives representative examples of glacier area and volume time series for the Mica basin study area. The simulated glacier area and volumes both show a decline into the 1950s followed by a decade-long levelling out. Glacier volume loss during the early 20<sup>th</sup> century is likely a response to warming climate following the end of the so-called Little Ice Age. In the 1960s through the 1970s, both glacier area and volume increase. The fairly substantial and rapid increase in ice covered area is surprising given the otherwise slow response time of glaciers. Much of the area gain is likely to be associated with the formation of new perennial snowfields rather than increases in glacier length. Volume, on the other hand, is probably being added in accumulation areas as well as newly formed snowfields. The volume change amounts to an increase of more than 20% during this period. After the mid-1970s both area and volume decline leading to the ongoing recession of glaciers in the Mica catchment. The transition from growth to shrinkage in the mid-1970s is widely noted to correspond with the change of phase of the PDO associated with a shift from less frequent ENSO negative years and more frequent ENSO positive years (Mantua *et al.* 1997). Such glacier variability, associated with naturally occurring climate oscillations, are expected to continue into the future. It is only with the century-long perspective that conclusions regarding glacier response to long-term anthropogenic climate change may be drawn.

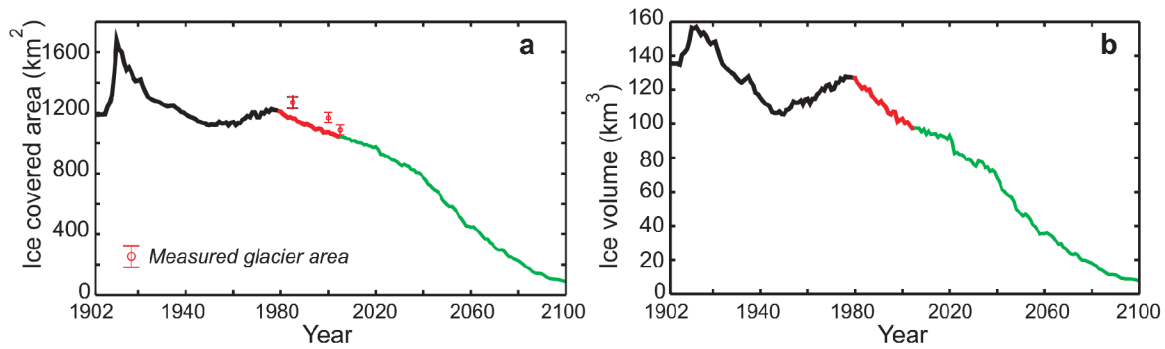


**Figure 6.1.** Computer simulated times series of glacier area and volume in the Mica Creek study area. For the interval 1902–1978 the climate forcing is derived from CRUTS2.1 (black curve); for 1979–2005 the climate forcing is from the NARR (red curve); for 2006–2100 the climate forcing is derived from the ECHAM GCM and the A1B emissions scenario (green curve). (a) Area time series. Measured glacier area is also indicated and agrees well with the simulated values. (b) Volume time series.

In Figure 6.1 the glacier area derived from satellite and aerial remote sensing by Bolch *et al.* (2010) is plotted along with the simulated glacier area. The simulated glacier area change is slightly less than the measured change and the absolute area is consistently less than that derived by Bolch *et al.* (2010) with an offset of roughly 100 km<sup>2</sup>, or ~10% of the total ice covered area in the Mica catchment. The glacier extents from 1985 are derived from a data set that was acquired over several years, so it is possible that the error bars on this area measurement should be larger than the 4% used in the plotting which was taken from Bolch *et al.* (2010). The 10% offset between model and measurement is still greater than the uncertainty in the calculated areas, so it appears that there is some bias in the glacier simulations which can probably be attributed to a bias in the glacier mass balance. As noted in Section 4.2.1, there was a fairly consistent bias toward low precipitation gradient in the precipitation downscale. Although an attempt was made to correct this, it may be manifest in the simulated glacier extents.



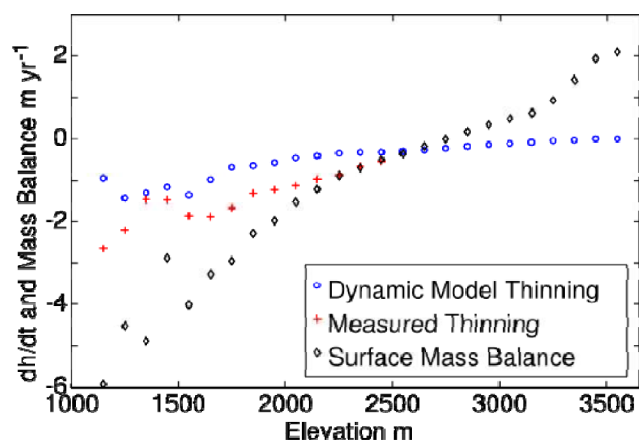


**Figure 6.2.** Vertical profiles of mass balance and thinning in the Mica catchment. The model results for mass balance are given as black diamonds, and the simulated dynamic thinning is shown as blue circles. Geodetic measurements of thinning are shown as red plus signs. The importance of capturing dynamic mass transfer is implicit in the dramatically different shape of the mass balance and the modelled thinning curves.

With regard to ice volume, Schiefer *et al.* (2007) estimated ice thickness changes between the TRIM and SRTM DEMs for mountainous regions across western Canada and determined specific annual thinning rates of  $0.64 \pm 0.15 \text{ m yr}^{-1}$  for the southern Rocky Mountains and  $0.53 \pm 0.13 \text{ m yr}^{-1}$  for the Columbia Mountains, which the Mica basin straddles. The modelling presented here simulates a specific annual thinning of  $0.30 \text{ m yr}^{-1}$ , which is less than that of either region including error estimates. Total volume loss over the period 1985–1999 is modelled at  $5.0 \text{ km}^3$  whereas the geodetically estimated volume change is  $7.8 \text{ km}^3$  with a specific thinning rate of  $0.43 \text{ m yr}^{-1}$  (B. Menounos, University of Northern British Columbia, unpublished data). Thus, while we expect a slight dry bias over the Mica catchment in our simulations, the actual volume changes are less than expected from measurements. This indicates that the dryness is partly offset by lower ablation rates in the mass balance model. It is possible that the reduced ice extent in the simulations leaves glaciers in a somewhat retreated position where they will experience lower rates of volume loss due to a lack of low elevation ice.

The vertical profiles of modelled surface mass balance and dynamic thickness change over the period 1985–1999 are presented in Figure 6.2. The simulated mass balance and thickness change differ markedly and as expected. The positive mass balance does not lead to thickening because ice flow transfers this mass to lower elevations. Mass transport results in thinning rates that are substantially lower than the mass balance rate. For example at elevations between 1000 m and 1500 m, the surface

mass balance is about  $-5$  m w.e.  $\text{yr}^{-1}$  whereas the thinning rate is closer to  $1.5$  m w.e.  $\text{yr}^{-1}$ . The thinning rate measured geodetically by Menounos (University of Northern British Columbia, unpublished data) compares well with the model results. The thinning is slightly greater, which agrees with the mean thinning rates discussed in the previous paragraph. Together these data indicate the necessity of incorporating glacier dynamics when making inferences about vertical profiles of mass balance from geodetically determined thinning rates.

## **6.2 21<sup>st</sup> century glacier projections**

### *6.1.1 Projected area change*

The area change associated with all scenarios and all GCMs is substantial. The best-case-for-glaciers scenario (CSIRO-B1) presents a reduction of 44% of the year 2000 ice covered area ( $1074 \text{ km}^2$ ) by 2100, but this is anomalous insofar as the next iciest scenario retained  $170 \text{ km}^2$  less ice cover. At worst case, several simulations show near-complete ice loss by 2100 (e.g., MIRO A1B). The dramatic extent of ice loss is exemplified by the mid-range ECHAM-A1B scenario, whose year 2000 and year 2100 masks are shown in Figure 6.3. This particular scenario exhibits a 92% loss of glacier cover. Such a large reduction in ice covered area results in near complete deglaciation of most regions with only the larger ice caps of the Rocky Mountains remaining at the end of 2100. The area changes for all GCMs and emission scenarios are summarized in Table 6.1. The projected change in glacier area is illustrated in Figure 6.4 which shows an oblique view of the changing ice mask and volume in 20 year increments from 2000 to 2100 as forced by the ECHAM A1B climate change scenario. The drastic loss of ice in the middle part of the century can be clearly seen.

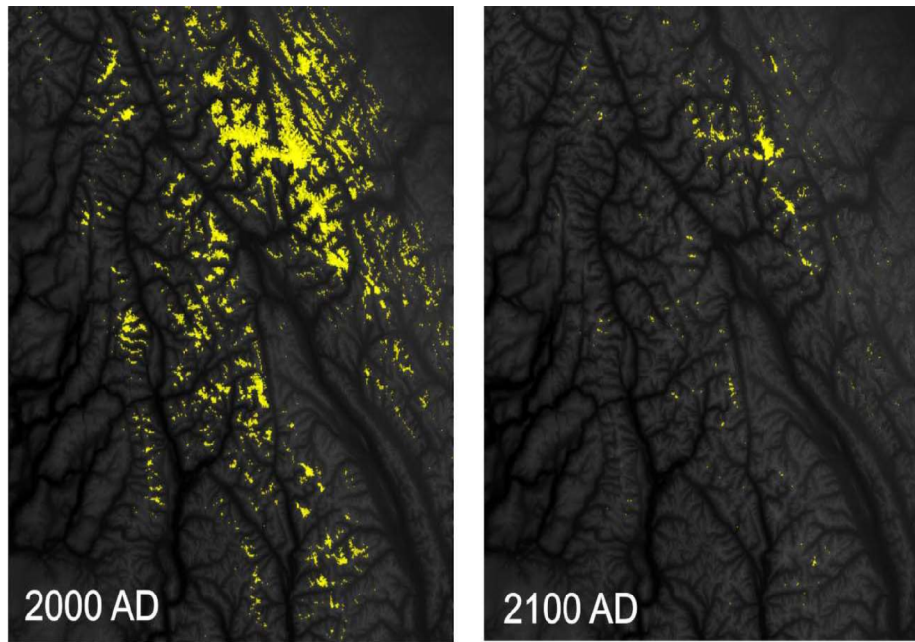


**Figure 6.3.** Simulated ice masks for the Mica basin region derived from the full model output. (a) Mask for 2000 AD using NARR and CRU climate forcing for 1900–2000 AD. (b) Mask for 2100 AD using ECHAM GCM output for the A1B scenario to represent the climate forcing for 2001–2100 AD.

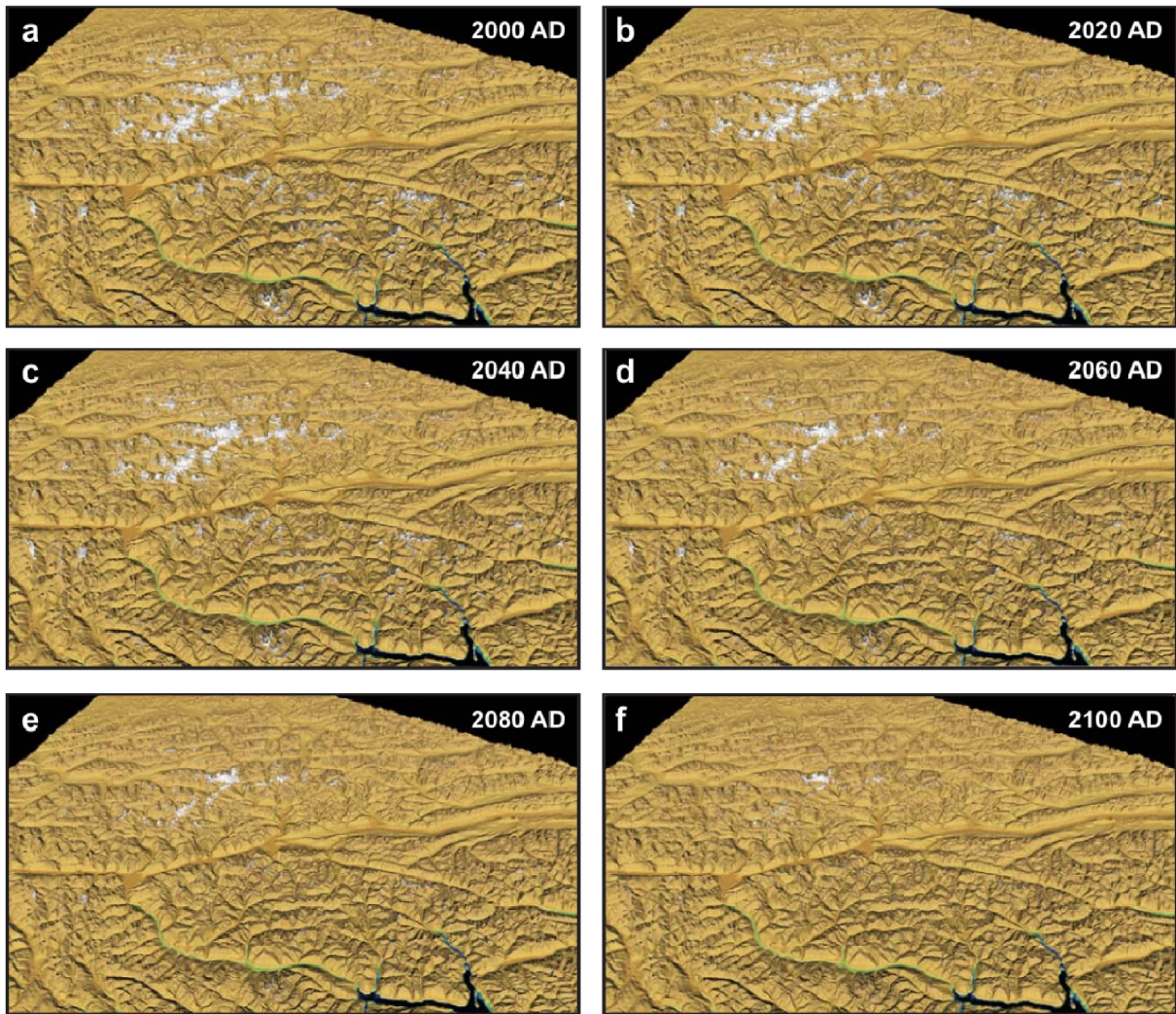


**Figure 6.4.** Example deglaciation simulation for Mica basin study region for 2000–2100 AD time interval. The model is forced using the ECHAM GCM and the A1B emissions scenario. The view is looking to the northeast so the Rocky Mountain Trench cuts across the images from left to right. Vertical exaggeration is 2 $\times$ .

Time series of glacier area for all GCMs and scenarios are given in Figure 6.5. For each scenario, there is a tendency for divergence after forcing with GCMs begins, and then convergence toward the end of the



simulations. Convergence occurs mainly because by 2100, much of the glacier area has been removed, forcing the results toward similarity at zero ice cover. This is most obvious for the A2 emissions scenario, which has the greatest warming of the three. Table 6.1 confirms that all GCMs in the A2 scenario (except the CSIRO GCM with 85% loss) force the loss of 90% or more of the simulated ice cover. The mean area loss for this emissions scenario is 93%. For the B1 emission scenario, the response of glaciers is quite varied. The minimum loss is from the CSIRO GCM with a 44% reduction in ice covered area while the MIRO CGM forces the loss of 97% of the year 2000 ice covered area. The mean area loss for the B1 scenario is 73%. As expected, the A1B scenarios fall in between these extremes with a mean area change of 89% although the MIRO GCM forces loss of almost 100% of glacier area by 2100 even under this moderate scenario.

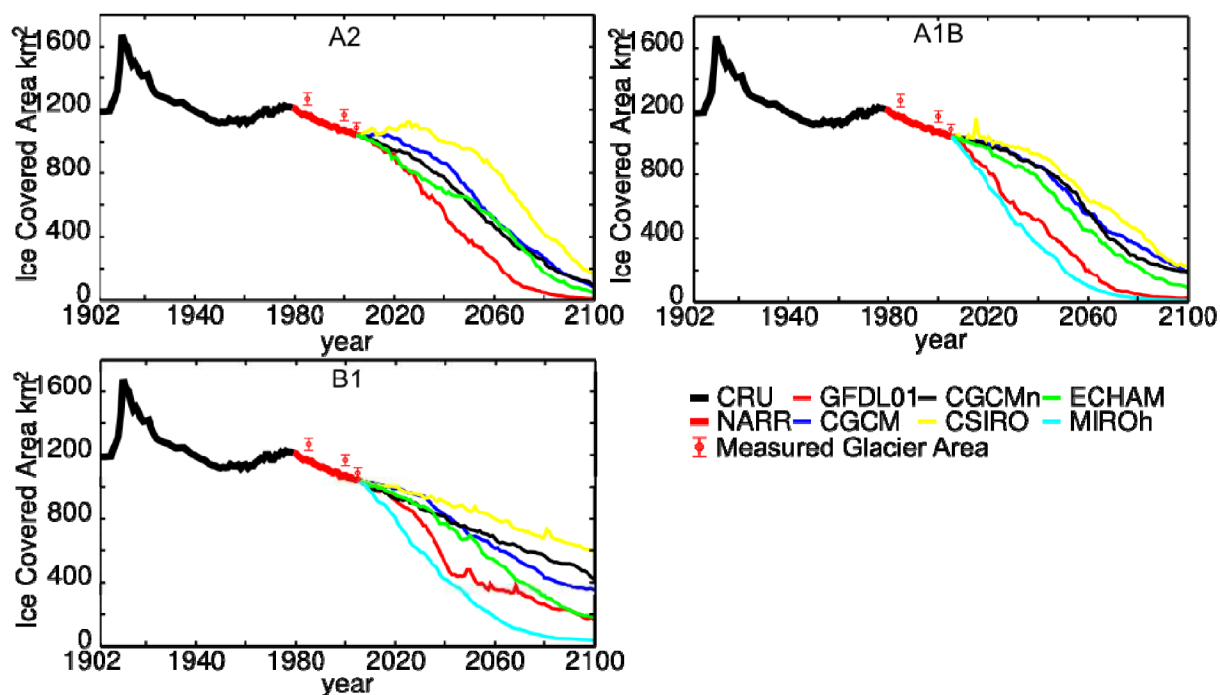


**Figure 6.5.** Time series of glacier area simulated for the Mica catchment using a variety of GCMs to provide projected climate forcing. The CRUTS2.1-based history is shown in heavy black and the NARR-based history is shown in heavy red. Remote sensing-based measurements of glacier area are shown in red symbols. (a) Results for A2 scenario. (b) Results for A1B scenario. (c) Results for B1 scenario. Note that forcing data from MIROh A2 were not available.

Substantial decadal variability in ice covered area is not apparent in the model results after year 2000. Most scenarios show a steady linear or exponential decay of ice cover moving asymptotically toward no ice. The exception to this is the CSIRO A2 scenario, which shows a strong increase in glacier cover

during the period 2000 through 2015. In the CSIRO A1B results, there is a shorter-period increase in glacier cover early in the record. By 2100 these result in the greatest ice-covered area of all GCMs for each scenario.

The peak positive and negative rates of area change have been calculated considering both the full period from 1920 (to avoid any spin-up transients) through 2100 and also for the period 2000 through 2100. These results are presented in the last four columns in Table 6.1. For most of the GCMs and scenarios the greatest positive and negative rates of area change occurred during the 20<sup>th</sup> century. That the greatest positive change in area occurs during the 20<sup>th</sup> century is not surprising given the decreasing likelihood of strongly positive mass balance years in a warming climate. For the most part, the year 1968 stands out as the year with greatest glacier expansion in the record for all but three of the GCM scenarios. The exceptions are CSIRO A1B, CSIRO B1, and GFDL B1. There are no strongly positive area increases for the A2 scenario due to the warm conditions associated with this scenario. In the 21<sup>st</sup> century perspective, for the A1B and A2 emission scenarios, all of the most positive rates of area change occur within the first three decades suggesting that as the climate warms further, any glacier advances are unlikely. Positive area changes occur later in the B1 scenario because that particular scenario foresees a decrease in the rate of warming to near zero by the latter part of the century making positive changes in glacier area possible once again.

For negative area change, the simulated very large decrease in area around 1922 is only matched by a few GCMs and emission scenarios (CSIRO A1B, GFDL A1B, and GFDL A2). It may seem surprising that the greatest rates of area loss occur in the 20<sup>th</sup> century while the greatest rates of warming occur in the 21<sup>st</sup> century. This is not the case if the fractional rate of change  $(1/A) dA/dt$  is considered. For the 21<sup>st</sup> century, the years with greatest fractional rates of area loss occur throughout the century, with no readily apparent tendency for these to occur earlier or later in the simulations. While not as great as the 1922 area loss, the rates are substantial. The greater loss in 1922 can be partly explained by the large size of glaciers at that time, when climate was warming from the cooler 19<sup>th</sup> century. The plotted area change time series (Figure 6.5) show a tendency for large negative rates of area reduction in the middle of the 21<sup>st</sup> century when the climate is hot and there is substantial ice cover to lose.

To compare the within-GCM difference, the area time series from all emission scenarios for the ECHAM GCM are plotted together in Figure 6.6. For this particular GCM, the between-scenario difference in the area projection is fairly small. This is confirmed by the data in Table 6.1 which show that the B1 scenario loses 83% of the year 2000 ice cover followed by A1B, which loses 92% and A2 which loses 96%. For

this GCM, the end result is as expected with the A2 and A1B scenarios retaining the least ice cover. The B1 scenario retains the greatest area throughout, while A1B and A2 trade positions.

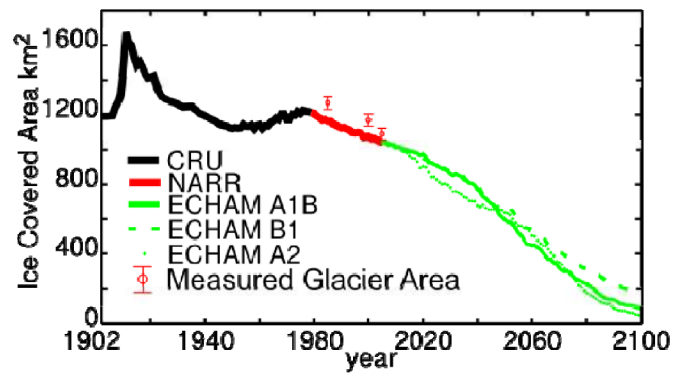


**Figure 6.6.** Time series of glacier area driven by the ECHAM climate change scenarios. The CRUTS2.1-based history is shown in heavy black and the NARR-based history is shown in heavy red. Remote sensing-based measurements of glacier area are indicated by red error-bar symbols.



**Table 6.1** Summary of area evolution for all GCMs and scenarios considered in this study.

Scenario	GCM	A <sub>2050</sub> km <sup>2</sup>	A <sub>2100</sub> km <sup>2</sup>	$\Delta A_{2100-2000}$ km <sup>2</sup>	$\Delta A_{2100-2000}$ %	Historical dA/dt max km <sup>2</sup> (year)	21 <sup>st</sup> Century dA/dt max km <sup>2</sup> (year)	Historical dA/dt min km <sup>2</sup> (year)	21 <sup>st</sup> Century dA/dt min km <sup>2</sup> (year)
A1B	CGCM	707	192	-882	-82%	31.6 (1968)	14.0 (2022)	-49.5 (1922)	-32.4 (2058)
	CGCMn	746	187	-887	-83%	31.6 (1968)	12.9 (2012)	-49.5 (1922)	-32.6 (2068)
	CSIRO	795	225	-849	-79%	124 (2015)	124 (2015)	-103 (2016)	-103 (2016)
	ECHAM	595	87.1	-987	-92%	31.6 (1968)	9.08 (2032)	-49.5 (1922)	-34.4 (2048)
	GFDL	355	17.4	-1060	-98%	31.6 (1968)	7.24 (2030)	-59.1 (2025)	-59.1 (2025)
	MIROh	210	5.4	-1070	-100%	31.6 (1968)	1.76 (2033)	-49.5 (1922)	-37.4 (2026)
Mean	–	568	119	-955	-89%	–	–	–	–
B1	CGCM	692	348	-725	-68%	31.6 (1968)	4.00 (2098)	-49.5 (1922)	-22.2 (2080)
	CGCMn	732	423	-653	-61%	31.6 (1968)	6.48 (2024)	-49.5 (1922)	-37.1 (2011)
	CSIRO	847	599	-474	-44%	48.1 (2081)	48.1 (2081)	-49.5 (1922)	-33.8 (2083)
	ECHAM	693	182	-892	-83%	31.6 (1968)	19.8 (2050)	-49.5 (1922)	-33.2 (2046)
	GFDL	479	163	-910	-85%	48.0 (2068)	48.0 (2068)	-49.5 (1922)	-48.4 (2069)
	MIROh	295	34.9	-1040	-97%	31.6 (1968)	0.24 (2087)	-49.5 (1922)	-37.6 (2038)
Mean	–	623	292	-782	-73%	–	–	–	–
A2	CGCM	691	82.8	-991	-92%	31.6 (1968)	9.04 (2011)	-49.5 (1922)	-31.6 (2055)
	CGCMn	612	90.6	-983	-92%	31.6 (1968)	5.96 (2022)	-49.5 (1922)	-29.2 (2057)
	CSIRO	959	161	-913	-85%	31.6 (1968)	25.2 (2017)	-49.5 (1922)	-37.9 (2064)
	ECHAM	637	47.0	-1030	-96%	31.6 (1968)	9.76 (2042)	-49.5 (1922)	-35.7 (2019)
	GFDL	367	7.1	-1070	-99%	31.6 (1968)	14.1 (2035)	-54.0 (2031)	-54.0 (2031)
Mean	–	653	77.6	-996	-93%	–	–	–	–

### 6.1.2 Projected volume change

In terms of volume, the results of our simulations are quite similar to the results for area change. The major difference is that volume is much more volatile than area. Increases in ice covered area requires a sufficient increase in mass balance to drive glacier termini to advance whereas volume changes can occur in response to individual large positive or negative mass balance years. Thus, a certain amount of interannual volume change may occur without any change in glacier area. Overall, the percentages of volume lost is slightly greater than the percentages of area lost by year 2100. For the A1B scenario, a mean of 90% of the year 2000 water equivalent ice volume ( $103 \text{ km}^3$ ) was lost amounting to  $92.9 \text{ km}^3$ . For the B1 and A2 scenarios, 76% and 93% of the ice volume was lost yielding  $78.2 \text{ km}^3$  and  $96.2 \text{ km}^3$  of water equivalent. Among the GCMs for a given emission scenario, the differences are smaller for volume than they were for area. This is evident from the data in Table 6.2 as well as in the volume time series plots given in Figure 6.7. This is especially true for the A1B and A2 emission scenarios for which ice volume converges to lower than 90% of the year 2000 amount for most of the GCMs. The CGCM models for the A1B scenario as well as the CSIRO model for both A1B and A2 are the exceptions. These GCM and scenario combinations result in very small volume changes for the first decade or two after year 2000.

The projected volume time series show a tendency for rapid volume change in mid-century when temperature is warm and there is still sufficient glacier area for melting. There is a sharp break in trend at the changecover from NARR to the climate change scenarios for several of the GCMs. For CGCM and CSIRO, the beginning of the 21<sup>st</sup> century shows reduced volume change for the first several decades. For the GFDL and MIRO models the tendency is for an abrupt increase of the rate of volume loss.

As was done with the area changes, the rates of change of volume were calculated and the maximum and minimum rates for the entire period, as well as exclusively for the 21<sup>st</sup> century, are reported in Table 6.2. The historical maximum in volume change, as simulated here, was for the year 1972 for most of the GCM and scenario combinations. However, half of the GCMs simulate a 21<sup>st</sup> century maximum for the A1B scenario and only the CSIRO simulations for the B1 and A2 scenarios have a 21<sup>st</sup> century volume change maximum. It is expected that there will be greater precipitation amounts under most emission scenarios, which is confirmed in the data used in this study (see Figure 4.3). Thus, for the early part of the 21<sup>st</sup> century, the moderate increases in precipitation combined with still relatively cool temperatures are able to generate anomalously positive volume changes. For the remaining GCMs and scenarios, the greatest

rates of volume change in the 21<sup>st</sup> century occur within the first few decades, further supporting the projection that late-century temperatures will make increases in glacier volume successively less likely.

**Table 6.2** Summary of volume evolution for all GCMs and scenarios considered in this study.

Scenario	GCM	V <sub>2050</sub> km <sup>3</sup>	V <sub>2100</sub> km <sup>3</sup>	ΔV <sub>2100-2000</sub> km <sup>3</sup>	ΔV <sub>2100-2000</sub> %	Historical dV/dt max (year) km <sup>3</sup>	21 <sup>st</sup> Century dV/dt max (year) km <sup>3</sup>	Historical dV/dt min (year) km <sup>3</sup>	21 <sup>st</sup> Century dV/dt min (year) km <sup>3</sup>
A1B	CGCM	58.3	15.3	-87.8	-85%	4.4 (2022)	4.4 (2022)	-5.7 (1998)	-4.3 (2044)
	CGCMn	63.9	16.7	-86.3	-84%	4.0 (2012)	4.0 (2012)	-5.7 (1998)	-4.7 (2039)
	CSIRO	64.2	18.3	-84.7	-82%	7.1 (2015)	7.1 (2015)	-6.3 (2009)	-6.3 (2009)
	ECHAM	46.9	7.8	-95.2	-92%	3.8 (1972)	3.2 (2032)	-7.1 (2022)	-7.1 (2022)
	GFDL	27.3	2.0	-101.0	-98%	3.8 (1972)	1.8 (2032)	-7.3 (2011)	-7.3 (2011)
	MIROh	16.9	0.6	-102.4	-99%	3.8 (1972)	0.8 (2033)	-5.7 (1998)	-5.5 (2009)
Mean	–	46.3	10.1	-92.9	-90%	–	–	–	–
B1	CGCM	56.2	30.1	-72.8	-71%	3.8 (1972)	2.1 (2018)	-5.7 (1998)	-4.5 (2033)
	CGCMn	65.5	32.9	-70.1	-68%	3.8 (1972)	2.6 (2024)	-8.6 (2011)	-8.6 (2011)
	CSIRO	75.7	52.9	-50.1	-49%	4.9 (2052)	4.9 (2052)	-5.7 (1998)	-4.8 (2067)
	ECHAM	58.7	15.9	-87.1	-85%	3.8 (1972)	2.8 (2012)	-5.7 (1998)	-5.1 (2042)
	GFDL	37.5	13.5	-89.5	-87%	3.8 (1972)	2.9 (2058)	-5.8 (2009)	-5.8 (2009)
	MIROh	22.9	3.5	-99.5	-97%	3.8 (1972)	0.6 (2031)	-5.7 (1998)	-4.5 (2009)
Mean	–	52.8	24.8	-78.2	-76%	–	–	–	–
A2	CGCM	55.1	7.1	-95.9	-93%	3.8 (1972)	2.4 (2011)	-5.7 (1998)	-5.1 (2023)
	CGCMn	48.4	7.6	-95.4	-93%	3.8 (1972)	2.6 (2022)	-5.7 (1998)	-4.2 (2027)
	CSIRO	91.7	13.4	-89.6	-87%	4.4 (2017)	4.4 (2017)	-5.7 (1998)	-5.2 (2064)
	ECHAM	58.6	4.8	-98.2	-95%	3.8 (1972)	3.3 (2008)	-5.7 (1998)	-6.1 (2019)
	GFDL	27.3	1.0	-102.0	-99%	3.8 (1972)	3.1 (2027)	-8.6 (2021)	-8.6 (2021)
Mean	–	56.2	6.7	-96.2	-93%	–	–	–	–

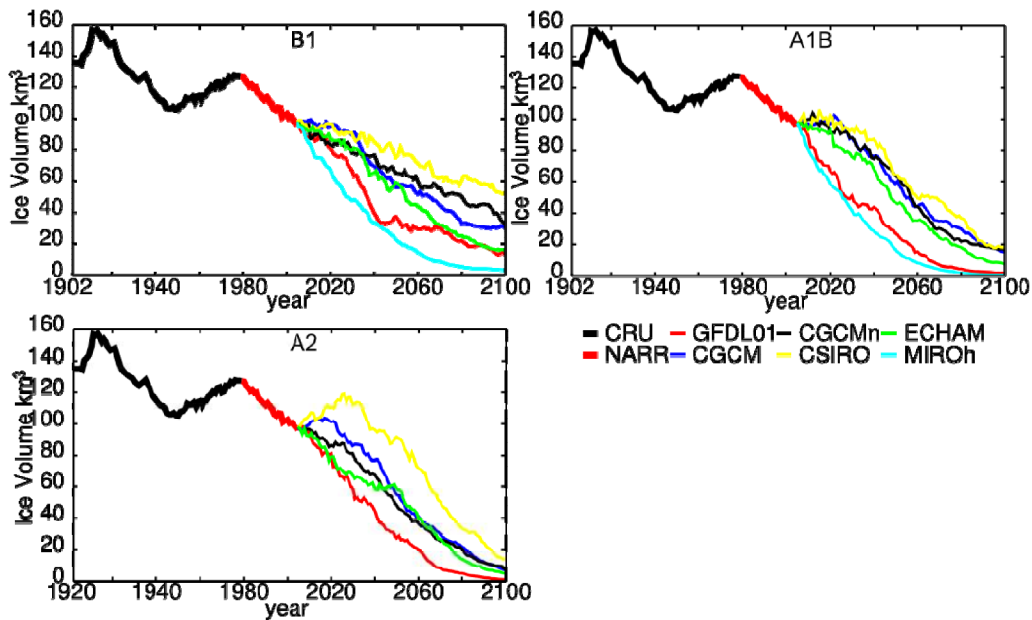


**Figure 6.7.** Time series of glacier volume simulated for the Mica catchment. The CRUTS2.1-based history is shown in heavy black and the NARR-based history is shown in heavy red. (a) Results for the A2 scenario. (b) Results for the A1B scenario. (c) Results for the B1 scenario. Note that forcing data from MIROH A2 were not available.

With respect to volume loss, the greatest rates occur late in the 20<sup>th</sup> century for more than half of the GCM and scenario combinations. Specifically, the 1998 volume change is the most negative for many of the scenarios. This mass balance year overlapped with one of the strongest El Niño events on record. However, for half of the GCM scenario combinations a more negative volume change year occurs later on in the simulations but almost always prior to the middle part of the 21<sup>st</sup> century, and most of these volume change anomalies are almost as large as that which occurred in 1998. Thus, although the total volume and areal coverage of glaciers shrinks dramatically throughout the century, the rate of warming is sufficiently fast that annual glacier volume reductions remain large within a historical context. Given the very extensive ice cover early in the 20<sup>th</sup> century, this amounts to very large rates of thinning unlike what we see today. This is visualized in Figure 6.8, which shows the 5-year smoothed rate of volume change through the simulation period. The 1920s and 1930s were characterized by large volume loss as somewhat extensive glaciers, which grew during the Little Ice Age, experienced warmer temperatures. In the 21<sup>st</sup> century, the rates of volume loss again increase. During this time, there is less ice area to experience melting overall, but the intensity of melting will be very high leading to rates of volume loss

equal to those seen early in the 20<sup>th</sup> century. This suggests that the specific thinning rates will be much higher and thus the melt intensity higher on the remaining glaciers.

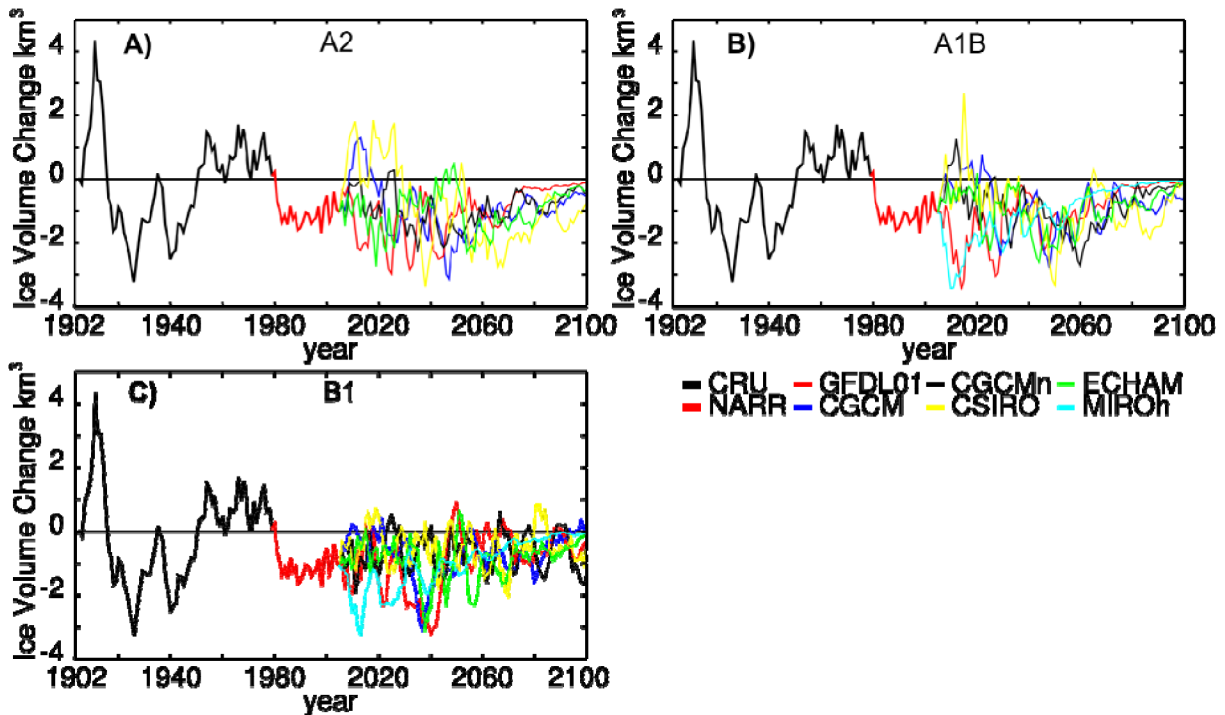


**Figure 6.8.** Simulated rate of volume change for the period 1902 through 2100 for the three emissions scenarios. Change rates are smoothed with a 5-year moving window. Results show that the high rates of volume loss over the past century will be reached again in the coming 100 years albeit with different timing for individual models and emission scenarios.

The differences between scenarios for a single GCM are also analyzed in terms of volume. This is shown in Figure 6.9 where the volume results for all scenarios of the ECHAM model are plotted. As before, there is no great difference between the scenarios for this GCM. The results from all emission scenarios show a decline in the rate of volume loss at the onset of the 21<sup>st</sup> century. The results from the A2 scenario resume high volume loss rates and result in the lowest remaining volume at the end of the century. The A1B scenario results show similar rates of volume loss to the results from the B1 scenario over the first 50 years of the projection. Thereafter, there is a very steep decline in ice volume, resulting in a near match to the end-of-century volume from the A2 scenario.

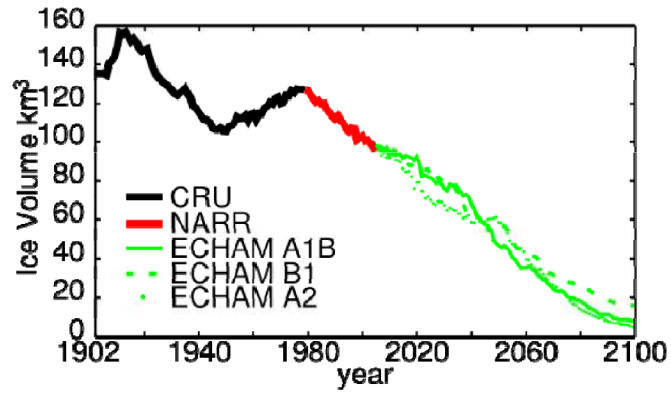


**Figure 6.9.** Time series of glacier volume driven by the ECHAM climate change scenarios. The CRUTS2.1-based history is shown in heavy black and the NARR-based history is shown in heavy red. Part of the explanation for the similarity among scenarios is that substantial ablation has already occurred in the Mica catchment before the GCM warming scenarios take effect.

## **7 Streamflow response to future climate scenarios**

### **7.1 Introduction**

This section presents the results of the streamflow projections. It focuses on three aspects: annual streamflow, which is especially relevant in systems with large reservoirs, such as Mica; August streamflow, because August is the month in which glacier runoff consistently provides a major contribution to flow (Stahl and Moore 2006); and the streamflow regime, as expressed by the variation of mean monthly streamflow through the year. Each available emission scenario for each GCM was simulated with all 23 behavioural parameter sets. The following results are based on the arithmetic mean of the 23 behavioural parameter sets (hereafter denoted as the "ensemble mean"). Seibert and Beven (2009), Houtekamer et al. (1996) and Krzysztofowicz (1999, 2001) showed that such ensemble predictions can outperform predictions using single parameter sets. In addition, in line with the assumption that all parameter sets are equally plausible for Mica basin, the predictions from all parameter sets are used to illustrate the range of potential streamflow scenarios. Because daily time series have been stored for all projections, it would be straightforward to expand the analysis to look at other aspects of streamflow changes, such as flows during specific times of year or annual peak and low flows.

### **7.2 Overview of weather forcing based on GCM output**

#### *7.2.1 GCMs and greenhouse gas emission scenarios*

Table 7.1 summarizes the selected GCMs and the available emission scenarios. Daily output for the period from 1961 to 2100 is available for two versions of the CGCM3.1 model and for run 4 of the A1B emission scenario for ECHAMS. For these GCM/emission scenario combinations, streamflow was simulated for the period from 1965-2100, with the preceding four years (1961-1964) used for model spin-up. Daily output for all other GCMs is available for the historic period 1961-2000 and two 20-year time slices, the first from 2046 to 2065 and the second from 2081 to 2100. The first four years of these time slices are used to spin up HBV-EC. Thus, hydrologic model simulations for future scenarios cover two 16-year time slices, the first spanning from 2050 to 2065 and the second from 2085 to 2100. In addition, the historic period from 1965 to 2000 was simulated using the respective historic forcings for each GCM/emission scenario combination.



**Table 7.1.** Emission scenarios and time span (time slice or full trajectory) for each selected GCM

GCM	Short name	Emission scenario	Timespan or slice*
CGCM3.1 (T47)	CGCMn	A2, A1B, B1	2000-2100
CGCM3.1 (T63)	CGCM	A2, A1B, B1	2000-2100
CSIRO-MK3.0	CSIRO	A1B, B1	2046-2065; 2081-2100
GFDL CM2.0	GFDL	A2, A1B, B1	2046-2065; 2081-2100
MIROC3.2 (hires)	MIRO	A1B, B1	2046-2065; 2081-2100
ECHAMS/MPI-OM	ECHAMS	A2, B1	2046-2065; 2081-2100
ECHAMS/MPI-OM	ECHAMS	A1B	2000-2100

\*historical streamflow simulations from 1965-2000. Historical baseline covers years from 1985-2000.

### 7.2.2 Description of the TreeGen downscaling approach

Daily weather sequences were downscaled from GCM output using the TreeGen downscaling algorithm, which was used by Stahl et al. (2008) to simulate glacier and streamflow responses to future climate scenarios in the Bridge River basin. TreeGen is a hybrid method that draws upon several approaches to statistical downscaling of GCM output, including regression modelling, analogue resampling and stochastic weather generation. In contrast to methods that use monthly GCM output, TreeGen preserves the sequencing of daily weather patterns as predicted by the GCMs, which can be important for controlling streamflow response.

The method can be divided into six steps. Models are estimated in steps 1 and 2. Once the model parameters have been identified, outputs from GCMs are downscaled in steps 3 to 6. Model estimation involves (1) common principal component analysis (PCA) of atmospheric reanalysis and GCM predictor fields for a baseline historical time period (Imbert and Benestad, 2005); and (2) synoptic map type classification of the common principal components (PCs) via a multivariate regression tree (MRT) (Cannon et al., 2002a, 2002b). Downscaled estimates of surface weather elements are then produced by (3) identifying future map types by entering the common PCs into the fitted MRT; (4) applying a nonparametric weather generator based on conditional resampling of temperature and precipitation data from each map type (Buishand and Brandsma, 2001); (5) estimating within-type interannual variability of temperature and precipitation at the nearest GCM grid point; and (6) adjusting the within-type interannual variability of the nonparametric weather generator using information from (5). Further details for each step are provided below.

Step 1: To mitigate potential biases between the atmospheric reanalysis and GCM simulated predictors,

common PCA is applied to the two data sets (Imbert and Benestad, 2005). First, predictors from the reanalysis and GCM – in this case large-scale sea-level pressure, surface temperature, and precipitation fields for the region between 202.5°E and 247.5°E and 30°N and 70°N – are standardized so that the time series for each grid point has zero mean and unit variance during a common 1961–2000 baseline period. Second, standardized data from the reanalysis and the GCM are concatenated to form a single data matrix. Third, PCA is applied to the correlation matrix of the concatenated predictors and PCs accounting for 95% of the original predictor variance are retained. Finally, common PC scores from the GCM are rescaled so that their means and variances in the simulated baseline period match observed values from the same period. To ensure consistency of the simulated seasonal cycle, rescaling is performed on each month separately.

Step 2: Next, synoptic map types are defined using a multivariate regression tree (MRT) model that recursively splits observed data into increasingly homogeneous groups on the basis of thresholds in the common PC scores (Cannon et al., 2002a, 2002b). Values of the thresholds are optimized so that the associated surface temperature and precipitation observations are placed into groups (or weather map types) that minimize within-group sums of squares error. Following Cannon et al. (2002a), 25 map types are identified for the study domain.

Step 3: Once thresholds have been identified using the historical record, common PC scores from the GCM scenarios are entered into the MRT. This results in each day from a scenario being assigned to one of the map types.

Step 4: Next, surface weather conditions on a given day are predicted using a nonparametric weather generator. The weather generator operates by conditionally resampling from cases assigned to a given day's map type (Buishand and Brandsma, 2001). The probability of randomly selecting the temperature and precipitation observed on a historical day  $i$  as the predicted values on day  $t$  is taken to be inversely proportional to the square of the Euclidean distance between the predicted values on the previous day  $t-1$  and historical values of the weather elements on day  $i-1$ . The selection is limited to the set of historical days assigned to the map type that is predicted to occur on day  $t$ .

Step 5: As the nonparametric weather generator in step 4 samples cases from the historical data set, future trends in surface climate conditions are due exclusively to changes in the frequency and timing of the synoptic map types simulated by the GCM. Additional processing is thus needed to accurately model trends and interannual variability occurring within each map type. In the original version of TreeGen

(Stahl et al., 2008), this is accomplished following the regression-based methodology described by Imbert and Benestad (2005). One potential drawback of this approach is its sensitivity to predictor selection, a problem that can lead to large differences in estimated climate change response for a given scenario (Huth, 2004). In this study, within-type trends are instead estimated directly from temperatures and precipitation amounts simulated at the nearest GCM grid point. For temperature, within-type differences from the 1961-2000 baseline period are calculated on an annual average basis for each map-type. The same is done for precipitation, except that annual averages are expressed as percentage changes with respect to the baseline.

Step 6: Finally, within-type interannual variability at the GCM grid point is superimposed onto the nonparametric weather generator outputs from step 4. Based on results from step 5, within-type corrections are applied on an annual basis for each map-type as additive bias corrections for temperature and multiplicative scaling factors for precipitation.

### 7.2.3 Comparison of historic and projected climate

Unless stated otherwise, we use the period from 1985 to 2000 as the historic baseline, a record of the same length as the projected 2050-2065 and 2085-2100 time slices. In all graphs that show stream discharge ( $Q$ ),  $Q$  for the historic period is based on simulations with the respective historic period for each GCM/emission scenario combination.. Because the glacier ice contribution to streamflow ( $Q_{ice}$ ) was not directly measured,  $Q_{ice}$  for the historic period is based on the ensemble mean of modelled  $Q_{ice}$ .

HBV-EC does not output a basin-average precipitation but only precipitation for each of the 500+ GRUs in the Mica basin. Therefore, to examine precipitation trends for the future climate scenarios, we averaged the downscaled projected climate forcing for all five climate stations in Mica and summarized projected changes. Tables 7.2 and 7.3 summarize trends in climate forcings relative to the downscaled GCM results for two historic periods, 1961-2000 (Table 7.2) and 1985-2000 (Table 7.3). Over the 21st century, precipitation is projected to vary from a slight decrease (CSIRO, B1) to up to a 25% increase (CGCM, A1B), depending on the GCM. For a given GCM, precipitation differences between emission scenarios are minor. Air temperature is predicted to increase by 1.4 °C to 5.6 °C relative to the 1985-2000 historical period (1.5 °C to 5.8 °C with 1961-2000 as a baseline), depending on the emission scenario and the length of the historic baseline.

**Table 7.2.** Historic (1961-2000) and projected climate forcing trends for each emission scenario and GCM averaged over all five climate stations in Mica basin. P is mean annual precipitation; T<sub>a</sub> is mean annual air temperature.

SRES	GCM	P (1961-2000)		P (2050-2065)		P (2085-2100)		T <sub>a</sub> (1961-2000)		T <sub>a</sub> (2050-2065)		T <sub>a</sub> (2085-2100)	
		[mm]	[mm]	[% change]	[mm]	[% change]	[mm]	[% change]	[°C]	[°C]	[increase °C]	[°C]	[increase °C]
B1	csiro	1113	1118	0	1236	11		3.2	4.5	1.3	4.7	1.5	
	miro	1166	1230	5	1250	7		3.1	6.5	3.4	7.7	4.7	
	gfdl	1108	1158	4	1221	10		3.0	5.1	2.1	5.2	2.2	
	echams	1137	1316	16	1249	10		3.0	4.5	1.6	6.2	3.2	
	cgcm	1160	1243	7	1293	12		3.0	5.4	2.4	5.9	2.8	
	cgcmn	1124	1237	10	1363	21		3.0	4.5	1.4	5.0	2.0	
	<b>Mean</b>	<b>1134.7</b>	<b>1216.9</b>	<b>7.2</b>	<b>1268.7</b>	<b>11.8</b>		<b>3.0</b>	<b>5.1</b>	<b>2.0</b>	<b>5.8</b>	<b>2.7</b>	
A2	gfdl	1132	1175	4	1142	1		2.9	5.3	2.3	7.2	4.2	
	echams	1165	1268	9	1303	12		3.0	5.1	2.1	7.4	4.4	
	cgcm	1155	1354	17	1423	23		3.1	6.0	2.9	7.5	4.4	
	cgcmn	1140	1252	10	1405	23		3.0	5.3	2.3	7.2	4.2	
	<b>Mean</b>	<b>1148.0</b>	<b>1262.0</b>	<b>9.9</b>	<b>1318.3</b>	<b>14.8</b>		<b>3.0</b>	<b>5.4</b>	<b>2.4</b>	<b>7.3</b>	<b>4.3</b>	
A1B	csiro	1143	1192	4	1233	8		3.0	4.3	1.3	5.2	2.1	
	miro	1161	1243	7	1325	14		3.0	6.9	3.9	8.8	5.8	
	gfdl	1117	1262	13	1246	12		3.0	4.9	1.9	6.7	3.7	
	echams	1138	1305	15	1319	16		3.0	5.4	2.4	6.8	3.7	
	cgcm	1134	1325	17	1418	25		3.0	5.7	2.6	6.4	3.4	
	cgcmn	1148	1278	11	1316	15		3.1	5.4	2.3	6.1	3.0	
	<b>Mean</b>	<b>1140.0</b>	<b>1267.4</b>	<b>11.2</b>	<b>1309.5</b>	<b>14.9</b>		<b>3.0</b>	<b>5.4</b>	<b>2.4</b>	<b>6.7</b>	<b>3.6</b>	

**Table 7.3.** Historic (1985-2000) and projected climate forcing trends for each emission scenario and GCM averaged over all five climate stations in Mica basin. P is mean annual precipitation; T<sub>a</sub> is mean annual air temperature.

SRES	GCM	P (1985-2000)		P (2050-2065)		P (2085-2100)		T <sub>a</sub> (1985-2000)		T <sub>a</sub> (2050-2065)		T <sub>a</sub> (2085-2100)	
		[mm]	[mm]	[% change]	[mm]	[% change]	[mm]	[% change]	[°C]	[°C]	[increase °C]	[°C]	[increase °C]
B1	csiro	1157	1118	-3	1236	7		3.3	4.5	1.2	4.7	1.4	
	miro	1156	1230	6	1250	8		3.2	6.5	3.3	7.7	4.5	
	gfdo	1114	1158	4	1221	10		3.1	5.1	2.0	5.2	2.2	
	echams	1144	1316	15	1249	9		3.0	4.5	1.6	6.2	3.2	
	cgcm	1151	1243	8	1293	12		3.3	5.4	2.1	5.9	2.6	
	cgcmn	1146	1237	8	1363	19		3.4	4.5	1.1	5.0	1.6	
	<b>Mean</b>	<b>1144.8</b>	<b>1216.9</b>	<b>6.3</b>	<b>1268.7</b>	<b>10.8</b>		<b>3.2</b>	<b>5.1</b>	<b>1.9</b>	<b>5.8</b>	<b>2.6</b>	
A2	gfdo	1095	1175	7	1142	4		3.1	5.3	2.2	7.2	4.1	
	echams	1189	1268	7	1303	10		3.0	5.1	2.1	7.4	4.4	
	cgcm	1141	1354	19	1423	25		3.4	6.0	2.6	7.5	4.2	
	cgcmn	1148	1252	9	1405	22		3.5	5.3	1.8	7.2	3.8	
	<b>Mean</b>	<b>1143.2</b>	<b>1262.0</b>	<b>10.4</b>	<b>1318.3</b>	<b>15.3</b>		<b>3.2</b>	<b>5.4</b>	<b>2.2</b>	<b>7.3</b>	<b>4.1</b>	
A1B	csiro	1167	1192	2	1233	6		3.1	4.3	1.2	5.2	2.0	
	miro	1137	1243	9	1325	16		3.2	6.9	3.7	8.8	5.6	
	gfdo	1106	1262	14	1246	13		3.1	4.9	1.8	6.7	3.5	
	echams	1124	1305	16	1319	17		3.1	5.4	2.3	6.8	3.7	
	cgcm	1138	1325	16	1418	25		3.4	5.7	2.3	6.4	3.1	
	cgcmn	1191	1278	7	1316	10		3.6	5.4	1.8	6.1	2.5	
	<b>Mean</b>	<b>1143.9</b>	<b>1267.4</b>	<b>10.8</b>	<b>1309.5</b>	<b>14.5</b>		<b>3.3</b>	<b>5.4</b>	<b>2.2</b>	<b>6.7</b>	<b>3.4</b>	

1

### 2 **7.3 Projected changes in mean annual streamflow**

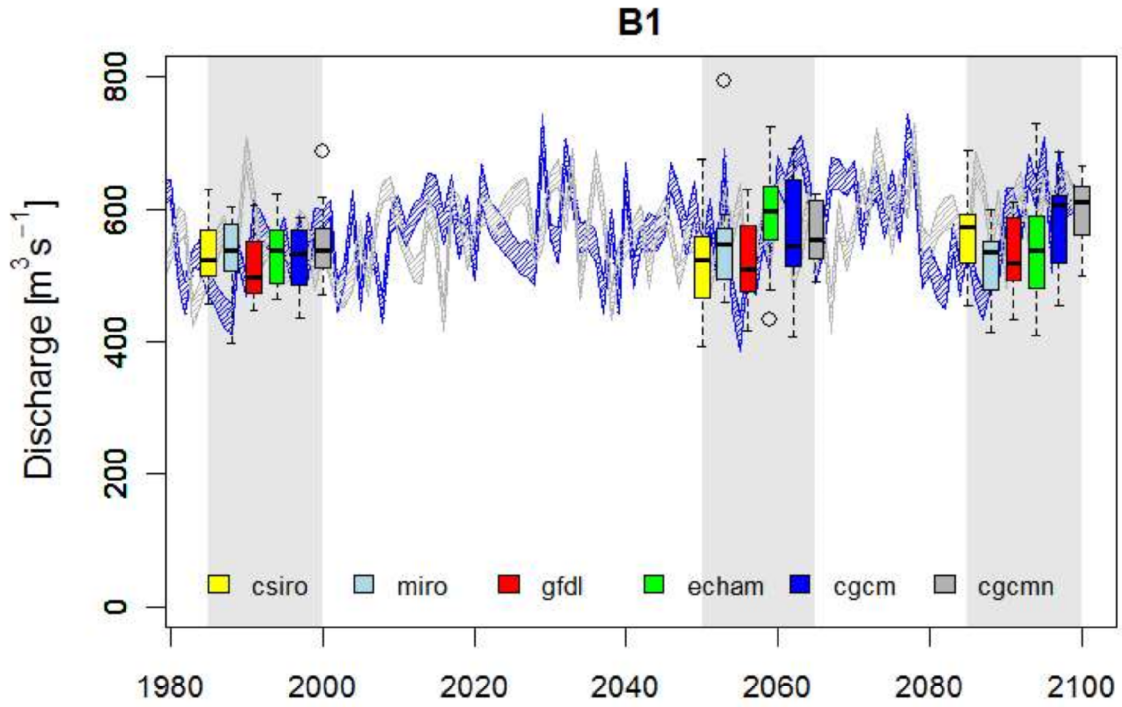
3

4 Figures 7.1, 7.2 and 7.3 summarize projections of mean annual streamflow for each scenario and the  
5 uncertainties associated with these projections relative to the historic baseline from 1985-2000. Historic  
6 streamflow scenarios are based on the downscaled output for each individual GCM/emission scenario  
7 combination to maintain consistency with the future projections. Trajectories are shown for models that  
8 cover the entire time span from 1985 to 2100 – i.e., CGCM (blue) and CGCMn (grey) for all scenarios  
9 and ECHAMS (green) for the A1B scenario. These trajectories are shown as bands that span the range of  
10 ensemble predictions based on the 23 parameter sets for each year, and thus illustrate the effects of  
11 parameter uncertainty. Distributions of annual streamflow for ensemble mean projections for each time  
12 slice and the historic baseline are shown in boxplots. For GCMs that cover the entire period 2000-2100,  
13 boxplots that summarize the time slices are given in the same color as for the respective trajectories.  
14 Tables 7.4 and 7.5 provide numerical summaries of the projected changes in mean annual flows and mean  
15 August streamflow for each scenario and each GCM.

16

17 Mean annual streamflow is projected to increase slightly in most emission scenario/GCM combinations.  
18 Due to higher evaporation rates and decreases in glacier ice melt, the increase in mean annual streamflow  
19 is lower than the increase in precipitation. CGCM generates the highest increase in mean annual  
20 streamflow in all scenarios. Amongst all scenarios, A1B generates the highest increase, with projections  
21 based on CGCM indicating an 18% increase in annual flow. Smaller flow increases are projected for the  
22 B1 scenario, while A2 and A1B result in similar increases in annual flow. The only GCM/emission  
23 scenario combinations that project a decreasing mean annual discharge are GFDL with the A2 scenario  
24 and CSIRO and MIRO with the B1 scenario. For many GCM/emission scenario combinations, the  
25 projected decreases in annual streamflow are of similar magnitude as the parameter uncertainty.  
26 Interannual variation in the 16-year time slices is larger than the annual flow changes in the mid 21<sup>st</sup>  
27 century and only slightly lower than the change towards the end of the 21<sup>st</sup> century.

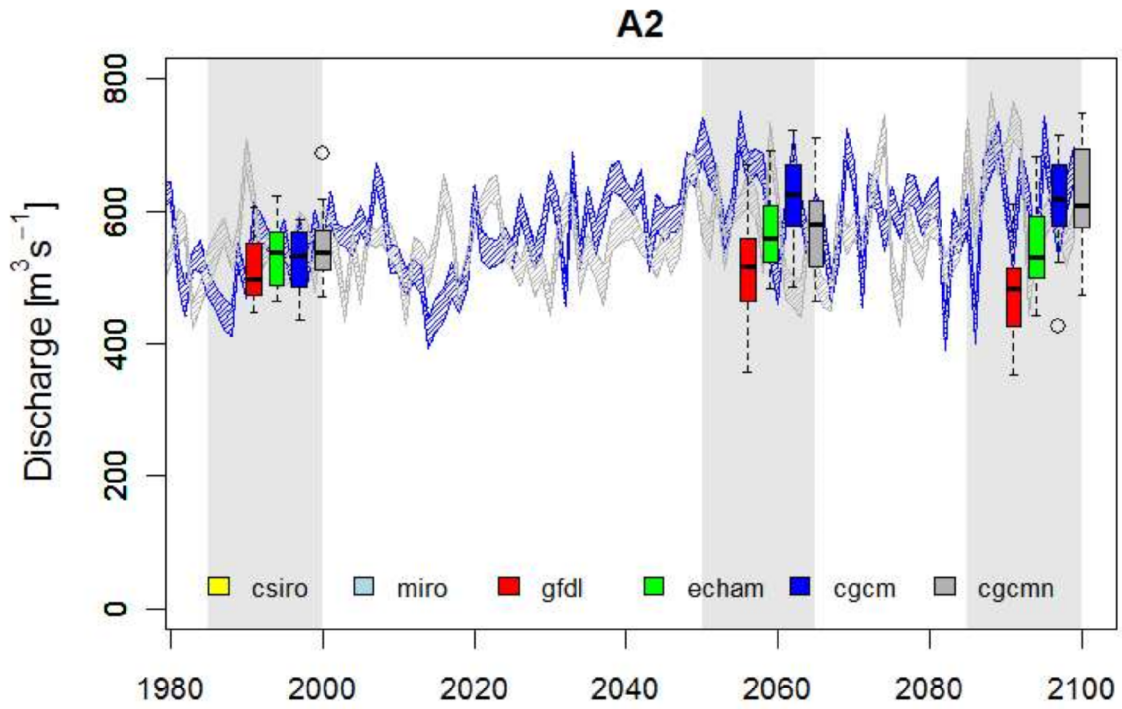
28



1  
2  
3  
4  
5  
6  
7

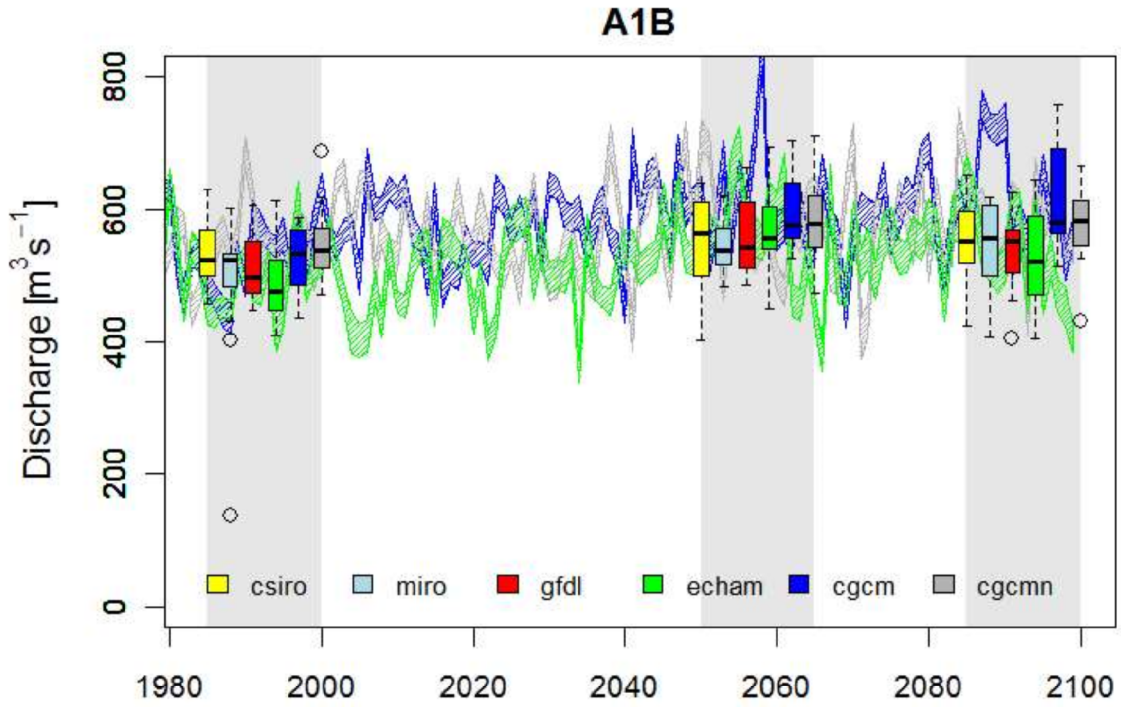
**Figure 7.1.** Historic values and projected changes in mean annual streamflow during the periods 2050-2065 and 2085-2100 for emissions scenario B1. Boxplots show the interannual variation of each time slice for each GCM, based on the ensemble mean of runs using all 23 behavioural parameter sets. Trajectories of ranges of ensemble predictions are shown for CGCMn (grey) and CGCM (blue).





1  
2  
3  
4  
5  
6  
7

**Figure 7.2.** Historic values and projected changes in mean annual streamflow during the periods 2050-2065 and 2085-2100 for emission scenario A2. Boxplots show the interannual variation of each time slice for each GCM, based on the ensemble mean of runs using all 23 behavioural parameter sets. Trajectories of ranges of ensemble predictions are shown for CGCMn (grey) and CGCM (blue).



1  
2  
3  
4  
5  
6  
7

**Figure 7.3.** Historic values and projected changes in mean annual streamflow during the periods 2050-2065 and 2085-2100 for emission scenario A1B. Boxplots show the interannual variation of each time slice for each GCM, based on the ensemble mean of runs using all 23 behavioural parameter sets. Trajectories of ranges of ensemble predictions are shown for CGCMn (grey), CGCM (blue), and ECHAM (green).

**Table 7.4.** Historic (1985-2000) and projected mean annual streamflow for each emission scenario and GCM.

Mean annual streamflow [m <sup>3</sup> /s]												
		1985 - 2000			2050 - 2065				2085- 2100			
SRES	GCM	Q	$\sigma_{IAV}^*$	$\sigma_{PU}^{**}$	Q	$\sigma_{IAV}^*$	$\sigma_{PU}^{**}$	$\Delta Q$ [%]	Q	$\sigma_{IAV}^*$	$\sigma_{PU}^{**}$	$\Delta Q$ [%]
B1	csiro	533.0	48.7	9.4	522.4	71.1	12.0	-2	561.4	64.8	11.8	5
	miro	528.4	61.2	9.4	545.9	79.2	12.7	3	517.1	50.5	12.4	-2
	gfdl	513.5	46.4	9.4	522.1	59.0	11.3	2	526.6	60.5	10.9	3
	echams	533.0	48.7	9.5	591.4	71.4	10.9	11	542.8	83.3	11.9	2
	cgcm	522.3	49.0	10.0	566.8	83.8	11.7	9	578.2	70.8	12.0	11
	cgcmn	546.2	51.9	10.6	560.1	45.5	10.3	3	599.2	46.7	10.6	10
	<b>Mean</b>	<b>529.4</b>	<b>51.0</b>	<b>9.7</b>	<b>551.4</b>	<b>68.3</b>	<b>11.5</b>	<b>4.2</b>	<b>554.2</b>	<b>62.8</b>	<b>11.6</b>	<b>4.7</b>
A2	gfdl	513.5	46.4	9.4	516.3	82.6	10.5	1	477.7	70.4	11.8	-7
	echams	533.0	48.7	9.5	566.3	64.8	11.0	6	561.2	104.5	13.3	5
	cgcm	522.3	49.0	10.0	623.1	65.9	13.2	19	612.8	77.9	13.6	17
	cgcmn	546.2	51.9	10.6	571.1	68.3	12.2	5	626.6	80.9	14.1	15
	<b>Mean</b>	<b>528.7</b>	<b>49.0</b>	<b>9.9</b>	<b>569.2</b>	<b>70.4</b>	<b>11.8</b>	<b>7.7</b>	<b>569.6</b>	<b>83.4</b>	<b>13.2</b>	<b>7.6</b>
A1B	csiro	533.0	48.7	9.4	549.4	76.2	11.1	3	551.7	67.8	11.6	3
	miro	493.1	105.8	9.0	543.7	39.5	12.6	10	548.7	61.9	13.1	11
	gfdl	513.5	46.4	9.4	559.4	60.8	11.7	9	532.7	57.6	12.3	4
	echams	486.5	50.5	10.5	561.5	70.4	16.8	15	527.6	68.4	17.4	8
	cgcm	522.3	49.0	10.0	607.0	81.6	12.9	16	618.8	81.0	12.9	18
	cgcmn	546.2	51.9	10.6	580.5	67.6	12.5	6	579.6	59.3	12.3	6
	<b>Mean</b>	<b>515.8</b>	<b>58.7</b>	<b>9.8</b>	<b>566.9</b>	<b>66.0</b>	<b>13.0</b>	<b>10.0</b>	<b>559.9</b>	<b>66.0</b>	<b>13.3</b>	<b>8.6</b>

\*  $\sigma_{IAV}$  is the standard deviation of projected streamflow, a measure of interannual variation (IAV).

\*\*  $\sigma_{PU}$  is the standard deviation of the ensemble of projections, a measure of parameter uncertainty (PU).

**Table 7.5.** Historic (1985-2000) and projected mean August streamflow for each emission scenario and GCM.

		Mean August runoff [m <sup>3</sup> /s]											
		1985 - 2000			2050 - 2065				2085- 2100				
SRES	GCM	Q	$\sigma_{IAV}^*$	$\sigma_{PU}^{**}$	Q	$\sigma_{IAV}^*$	$\sigma_{PU}^{**}$	$\Delta Q$ [%]	Q	$\sigma_{IAV}^*$	$\sigma_{PU}^{**}$	$\Delta Q$ [%]	
B1	csiro	913.2	162.3	28.2	729.4	193.7	36.1	-20	716.1	132.8	36.9	-22	
	miro	883.3	200.6	31.7	389.5	74.9	27.5	-56	274.9	46.2	18.4	-69	
	gfdl	867.4	153.8	28.7	627.7	180.9	38.3	-28	542.6	173.4	33.7	-37	
	echams	872.3	137.6	29.5	727.4	167.5	36.5	-17	543.4	174.7	28.8	-38	
	cgcm	788.0	135.9	31.3	711.5	172.0	33.2	-10	608.3	135.3	34.7	-23	
	cgcmn	864.8	130.0	34.7	740.7	113.7	34.3	-14	755.3	142.1	30.7	-13	
	<b>Mean</b>	<b>864.8</b>	<b>153.4</b>	<b>30.7</b>	<b>654.4</b>	<b>150.5</b>	<b>34.3</b>	<b>-24.1</b>	<b>573.4</b>	<b>134.1</b>	<b>30.6</b>	<b>-33.5</b>	
A2	gfdl	867.4	153.8	28.7	578.8	180.4	38.7	-33	289.7	117.1	35.1	-67	
	echams	872.3	137.6	29.5	700.8	217.5	33.2	-20	458.7	147.5	29.7	-47	
	cgcm	788.0	135.9	31.3	741.0	138.9	37.2	-6	537.1	142.7	38.9	-32	
	cgcmn	864.8	130.0	34.7	654.7	176.3	36.5	-24	527.9	188.6	42.6	-39	
	<b>Mean</b>	<b>848.1</b>	<b>139.3</b>	<b>31.1</b>	<b>668.8</b>	<b>178.3</b>	<b>36.4</b>	<b>-20.8</b>	<b>453.3</b>	<b>149.0</b>	<b>36.6</b>	<b>-46.2</b>	
A1B	csiro	913.2	162.3	28.2	847.7	193.6	37.2	-7	669.1	183.3	41.8	-27	
	miro	805.1	177.9	30.9	352.4	89.9	29.4	-56	256.8	65.7	17.0	-68	
	gfdl	867.4	153.8	28.7	638.9	246.5	51.1	-26	408.4	152.5	38.4	-53	
	echams	780.6	120.8	25.8	618.8	235.9	33.8	-21	459.4	89.3	29.5	-41	
	cgcm	788.0	135.9	31.3	715.2	199.7	34.4	-9	651.5	182.5	34.4	-17	
	cgcmn	864.8	130.0	34.7	698.7	161.7	38.1	-19	548.8	134.5	37.7	-37	
<b>Mean</b>	<b>836.5</b>	<b>146.8</b>	<b>29.9</b>	<b>645.3</b>	<b>187.9</b>	<b>37.3</b>	<b>-23.2</b>	<b>499.0</b>	<b>134.6</b>	<b>33.2</b>	<b>-40.5</b>		

\*  $\sigma_{IAV}$  is the standard deviation of projected streamflow, a measure of interannual variation (IAV).

\*\*  $\sigma_{PU}$  is the standard deviation of the ensemble of projections, a measure of parameter uncertainty (PU).

#### **7.4 Projected change of mean August flows**

Figures 7.4, 7.5 and 7.6 illustrate projections for all three emission scenarios and all 6 GCMs for August streamflow; Tables 7.4 and 7.5 provide numerical summaries. Projections for all three emission scenarios and all GCMs indicate substantial decreases in August streamflow in both the 2050-2065 and the 2085-2100 time slices. Depending on the scenario, changes between -6% and -56% are projected for the period 2050-2065 and between -13% and -69% for the period 2085-2100 (Tables 7.4 and 7.5).

The B1 scenario generates the smallest decreases in August streamflow. Most of the decline occurs in the first half of the 21<sup>st</sup> century; August streamflow continues to decline but at a slower rate in the second half of the 21<sup>st</sup> century. For all GCMs except MIRO, projected August streamflow for the 2050-2065 period agrees within 50 m<sup>3</sup>/s. The change in discharge relative to the historic baseline varies between -10 to -54%, depending on the GCM. CGCM produces the smallest decrease, followed by ECHAMS and CGCMn. For the 2085-2100 time slice, GCMs project decreases in mean August streamflow between -13% and -69%.

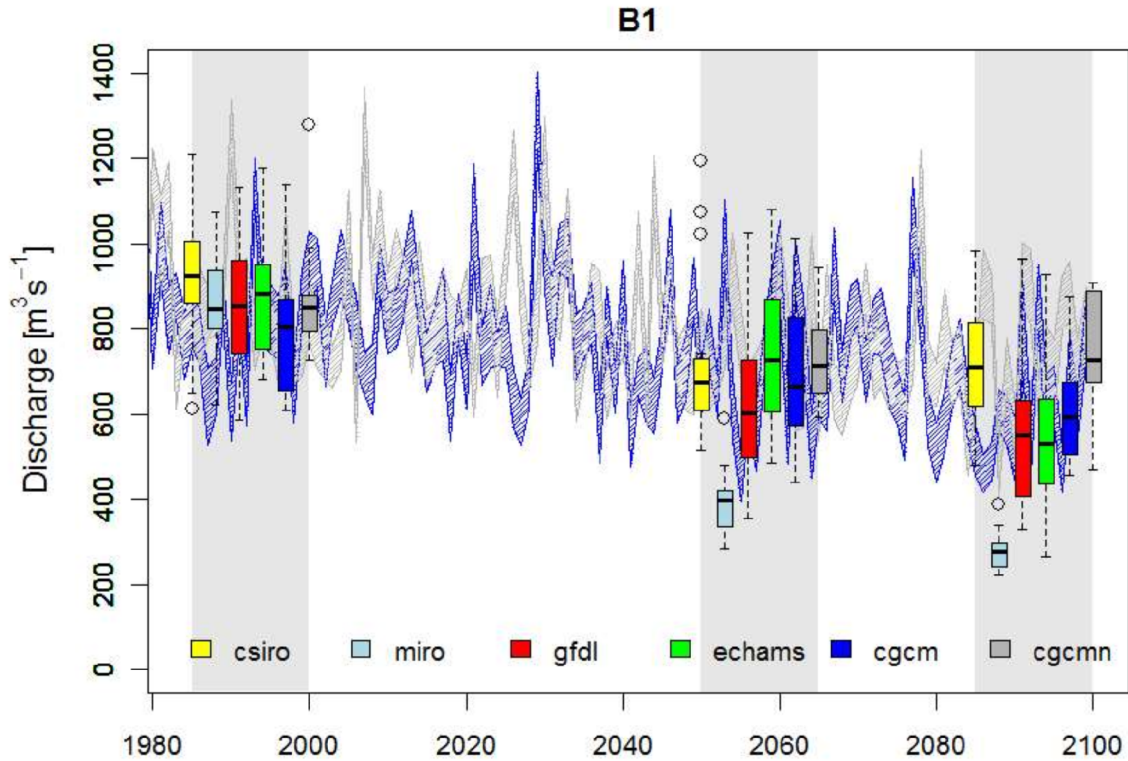


**Figure 7.4.** Historic values and projected changes in mean August streamflow during the periods 2050-2065 and 2085-2100 for emission scenario B1. Boxplots show the interannual variation for each time slice for each GCM, based on the ensemble mean of runs using all 23 behavioural parameter sets. Trajectories of ranges of ensemble predictions are shown for CGCMn (grey), CGCM (blue).

The highest projected decreases in mean August streamflow occur under the A2 emission scenario. Mean August streamflow is projected to decrease through the entire 21<sup>st</sup> century, with mean decreases of -19% and -46% in the 2050-2065 and 2085-2100 periods, respectively. Variation between the models is low, particularly for the 2085-2100 time slice. Note that the mean over all GCMs for A2 cannot be directly compared to those for the B1 and A1B scenarios because of the absence of MIRO and CSIRO runs.

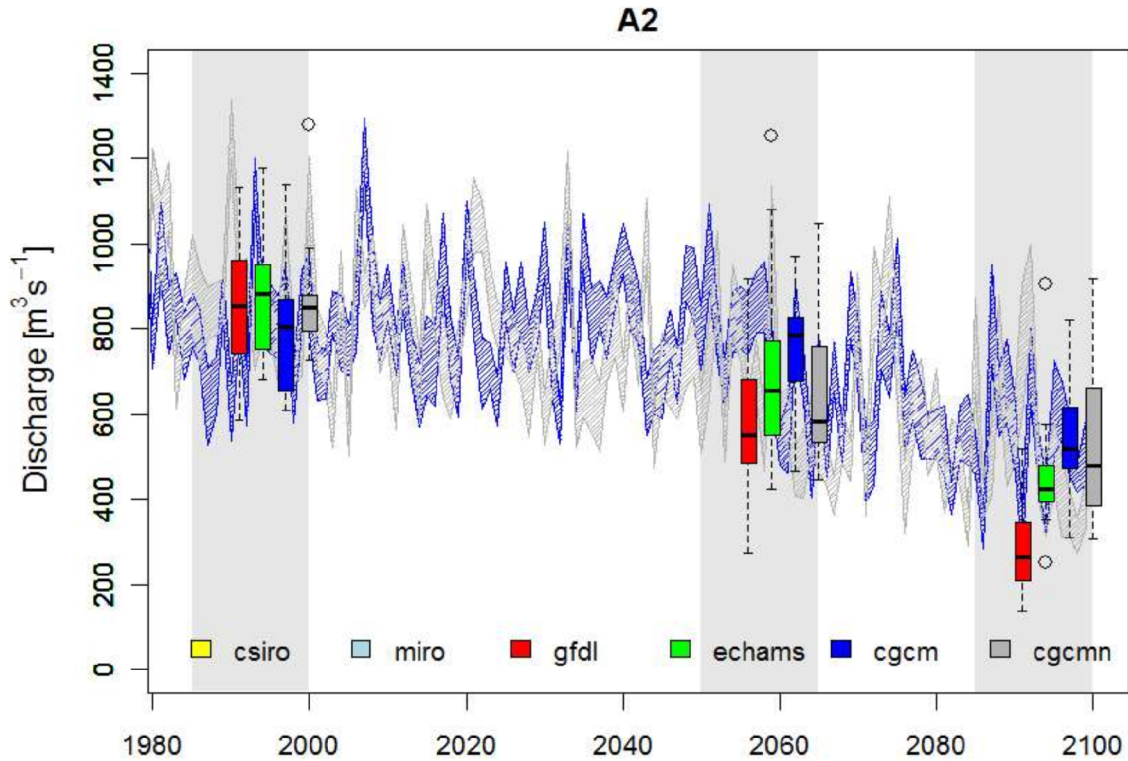


**Figure 7.5.** Historic values and projected changes in mean August streamflow during the periods 2050-2065 and 2085-2100 for emission scenario A2. Boxplots show the interannual variation for each time slice for each GCM, based on the ensemble mean of runs using all 23 behavioural parameter sets. Trajectories of ranges of ensemble predictions are shown for CGCMn (grey) and CGCM (blue).

Mean August streamflow under the A1B emission scenario is projected to gradually decrease over time with slightly more streamflow than under the A2 emission scenario. The variation among the various GCMs is higher than under the A2 scenario. Under the A1B scenario, mean August streamflow is projected to decrease by -23% and -40% in the 2050-2065 and 2085-2100 periods, respectively.



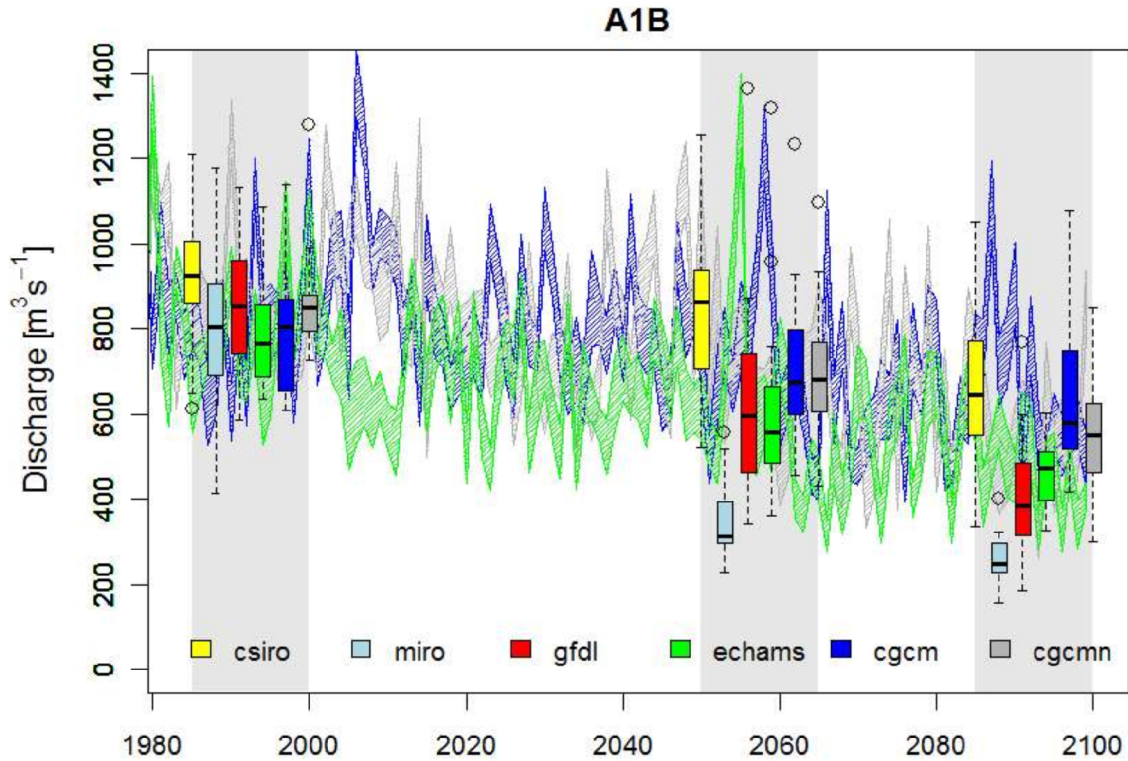


**Figure 7.6.** Historic values and projected changes in mean August streamflow during the periods 2050-2065 and 2085-2100 for emission scenario A1B. Boxplots show the interannual variation for each time slice for each GCM, based on the ensemble mean of runs using all 23 behavioural parameter sets. Trajectories of ranges of ensemble predictions are shown for CGCMn (grey) and CGCM (blue), and ECHAM (green).

## 7.5 Projected changes to streamflow regime

Figure 7.7 summarizes projected changes to the seasonal streamflow regime for the 2050-2065 and the 2085-2100 time slices. Despite the substantial uncertainties in the projections, shown hereafter, there is an unambiguous general trend towards higher discharges in early spring and lower discharges from July to September, and higher flows during the winter months (Figure 7.7). This is true for all emission scenarios and all GCMs. Projected changes to seasonal streamflow regime for the 2050-2065 period are similar under all emission scenarios (blue solid, dashed and dotted lines in Figure 7.7). For the 2085-2100 period, the mean over all GCMs for scenario A2 (solid red line in Figure 7.7) shows the most dramatic change, although this is also partly caused by the absence of projections based on the MIRO and CSIRO output for the A2 scenarios, which shifts the mean closer to models that project more dramatic changes to

streamflow such as ECHAMS (as will be shown later). The smallest changes to seasonal streamflow can be expected under the B1 scenario (dotted lines in Figure 7.7). The mean over all GCMs for the A1B scenario is close to that of the A2 scenario for August streamflow, but projections based on the A1B scenario do not exhibit as large a shift to increased runoff in early spring.

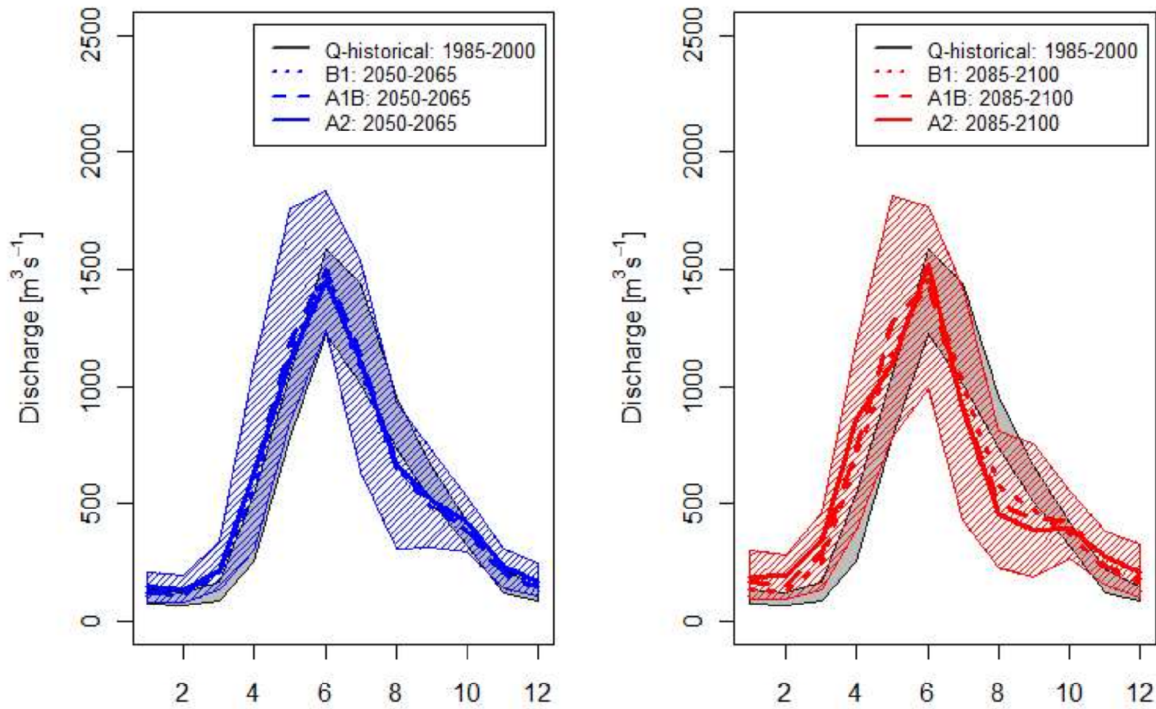


**Figure 7.7.** Historic and projected seasonal streamflow response for 2050-2065 (left) and 2085-2100 (right) time slices. The dashed areas (blue = 2050-2065; red = 2085-2100) cover the range of uncertainties associated with variation among GCMs and emission scenarios, and with parameter estimation for HBV-EC. Solid, dotted, and dashed lines show means for B1, A2, and A1B emission scenario over all GCMs (blue = 2050-2065; red = 2085-2100).

Figures 7.8, 7.9 and 7.10 split the overall variability shown in Figure 7.7 into the three emission scenarios. The dashed areas, blue for the 2050-2065 and red for the 2085-2100 time slice, mark the range of projections and reflect the uncertainties associated with variations among GCMs and the uncertainties associated with parameter estimation for HBV-EC. The ranges for each month of the year are calculated from minimum and maximum values over all GCMs, and all parameter sets (for a total of 6 x 23 HBV-EC runs for B1 and A1B and 4 x 23 for A2). For scenario B1, the projections based on output from CSIRO, GFDL, and CGCMn indicate the smallest shifts towards earlier flows and decreases in summer

flow. Greater shifts in seasonal flow regime are projected from forcings by MIRO, ECHAMS and to a lesser extent CGCM. Projections based on all GCMs except ECHAMS indicate marginal differences between the 2050-2065 and the 2085-2100 time slices.

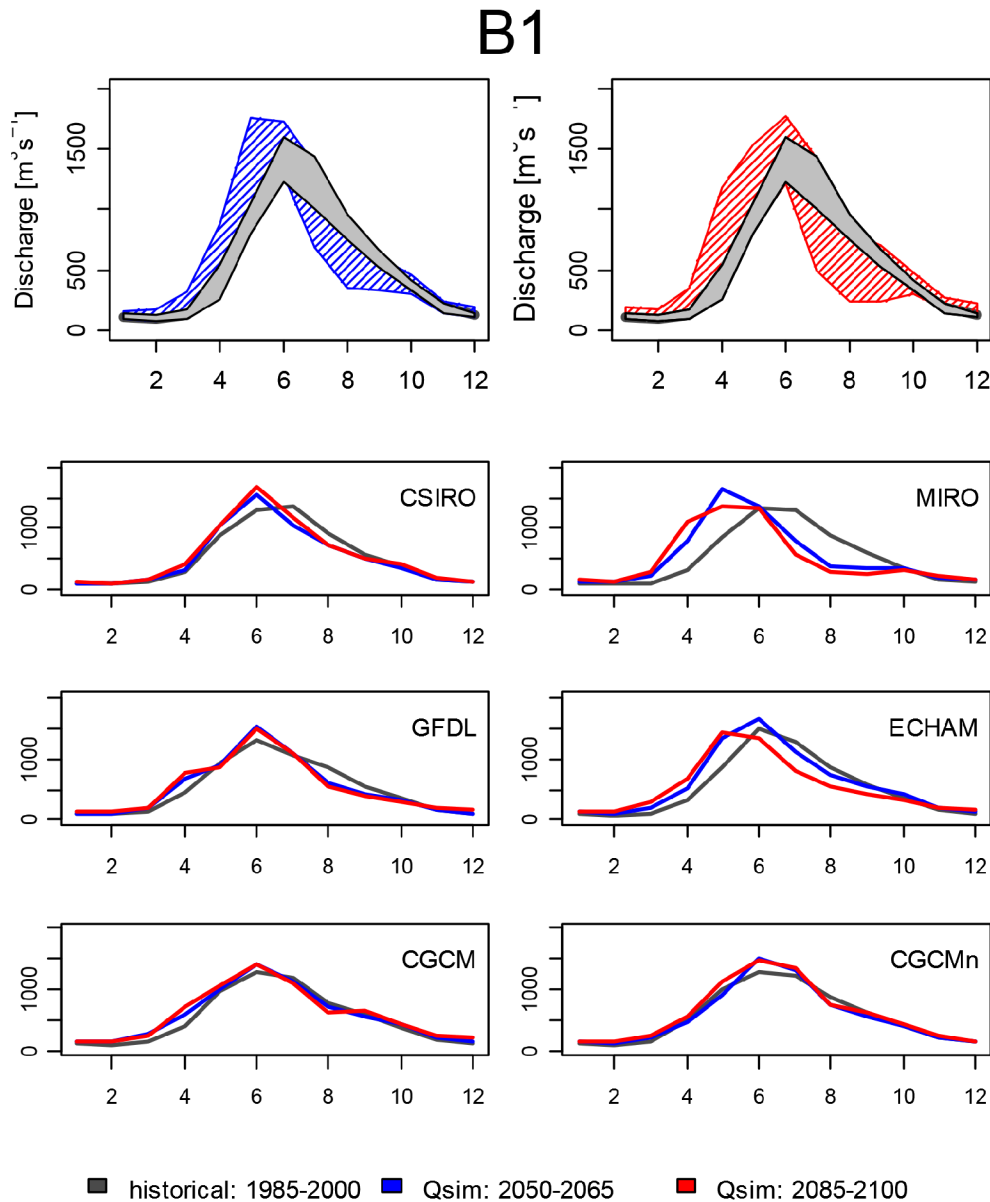


**Figure 7.8.** Projected seasonal streamflow response under the B1 scenario for 2050-2065 (blue) and 2085-2100 (red) time slices compared to historic baseline (black). Top: ensemble range for historic baseline runs (grey) compared to 2050-2065 time slice (top left) and to 2085-2100 time slice (top right) Bottom graphs: ensemble means (23 parameter sets) for 2050-2065 (blue) and 2085-2100 (red) time slices for each GCM.

Under the A2 scenario, projections based on all GCMs indicate substantial changes to the streamflow regime. Compared to the B1 and also the A1B scenario (shown below), considerable changes are projected for the 2085-2100 period compared to the 2050-2065 period (note that CSIRO and MIRO runs are not available for A2). Peak monthly runoff is projected to shift by one to two months from June/July in the historic period to May in the 2085-2100 time slice when HBV-EC is forced with ECHAMS or CGCMn output. Under scenarios forced by ECHAMS, CGCM and CGCMn, a small amount of glacier cover persists to the end of the 21<sup>st</sup> century, while glaciers have essentially disappeared under the A2 scenario forced by GFDL. This difference in projected glacier coverage is visible in the hydrographs: projections based on GFDL forcing show very low flows throughout the summer months due to the lack of contribution from ice melt.

## A2

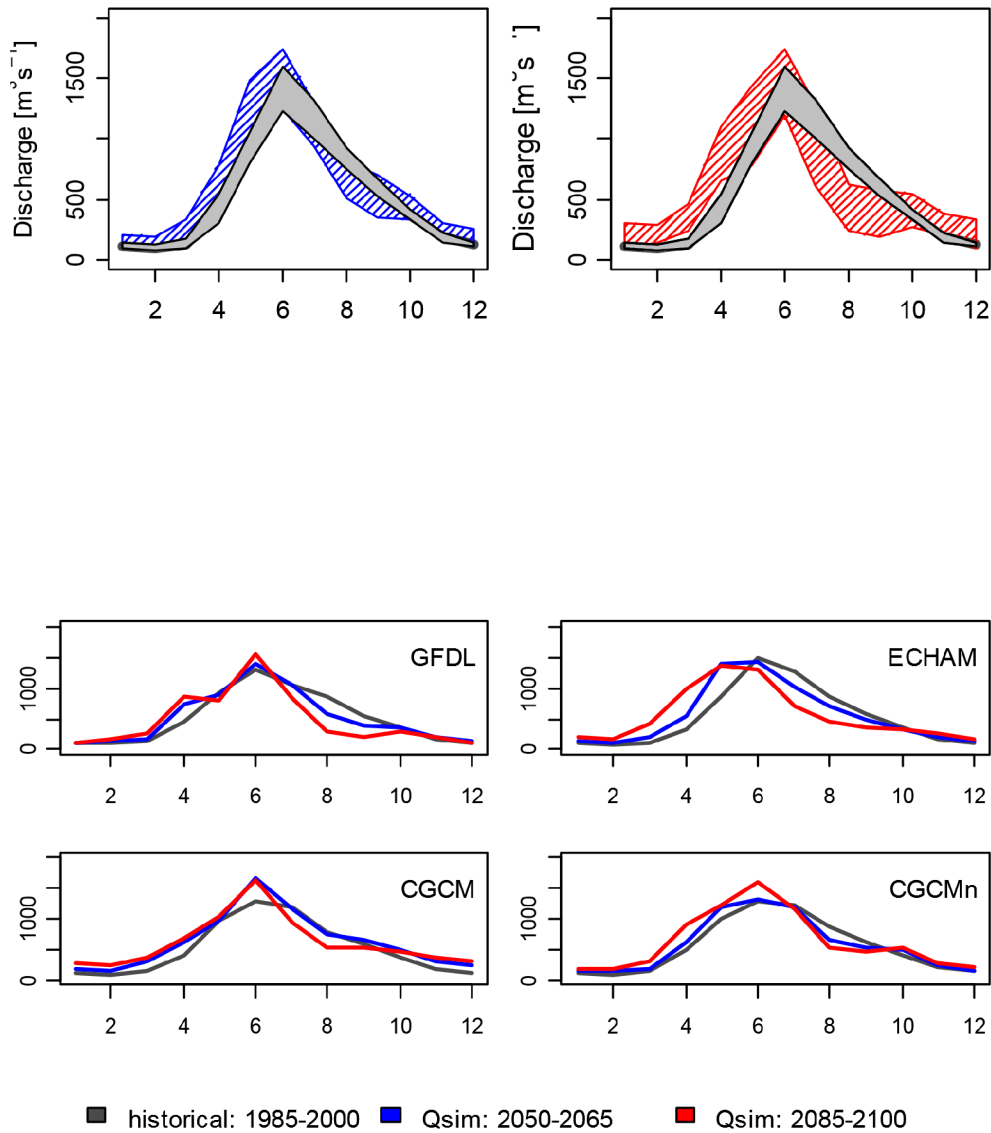


**Figure 7.9.** Projected seasonal streamflow response under the A2 scenario for 2050-2065 (blue) and 2085-2100 (red) time slices compared to historic baseline (black). Top: ensemble range of historic baseline runs (grey) compared to 2050-2065 time slice (top left) and compared to 2085-2100 time slice (top right) Bottom graphs: ensemble means (23 parameter sets) of 2050-2065 (blue) and 2085-2100 (red) time slices for each GCM.

Under the A1B emission scenario, changes in the 2050-2065 period are similar to those projected under the A2 scenario (considering the same four GCMs). However, the changes from 2050-2065 to 2085-2100

are less marked than under the A2 scenario, and are mainly restricted to decreasing summer flows with only marginal changes to the timing of peak monthly runoff. This results from the steadily decreasing glacier area under all GCM forcings and the gradually decreasing contribution of glacier ice melt to streamflow in the summer months. ECHAMS forcing produces the highest shift (~ two months) in the timing of peak flows. MIRO predicts the highest increase in peak monthly runoff, occurring in June, and brackets the maximum peak runoff that can be expected under all emission scenarios and GCMs.

## **7.6 Changes to ice melt contributions to streamflow**

Streamflow contributions from ice melt ( $Q_{ice}$ ) were extracted from HBV-EC output and compared to the range of historic contributions of  $Q_{ice}$  from all GCM/emission scenario combinations. These values represent the runoff generated each year by melting of glacier ice following disappearance of the snowpack. It is thus a measure of the contribution to streamflow over and above that by seasonal snowmelt or rainfall. Figure 7.11 illustrates the substantial uncertainties in projected contributions of glacier ice melt ( $Q_{ice}$ ) to streamflow. For the 2050-2065 time slice (Figure 7.11, left), projected  $Q_{ice}$  ranges from 20 to 250 m<sup>3</sup>/s. Given the low projected flows in August,  $Q_{ice}$  can contribute as much as half of the mean August flows. It is notable that future predictions of  $Q_{ice}$  never exceed the upper range of historical contributions of  $Q_{ice}$ . Towards the end of the 21<sup>st</sup> century, all GCMs project a decrease in  $Q_{ice}$  relative to the mid-21<sup>st</sup> century, with some models (e.g. GFDL) projecting only marginal contributions by  $Q_{ice}$ .

# A1B

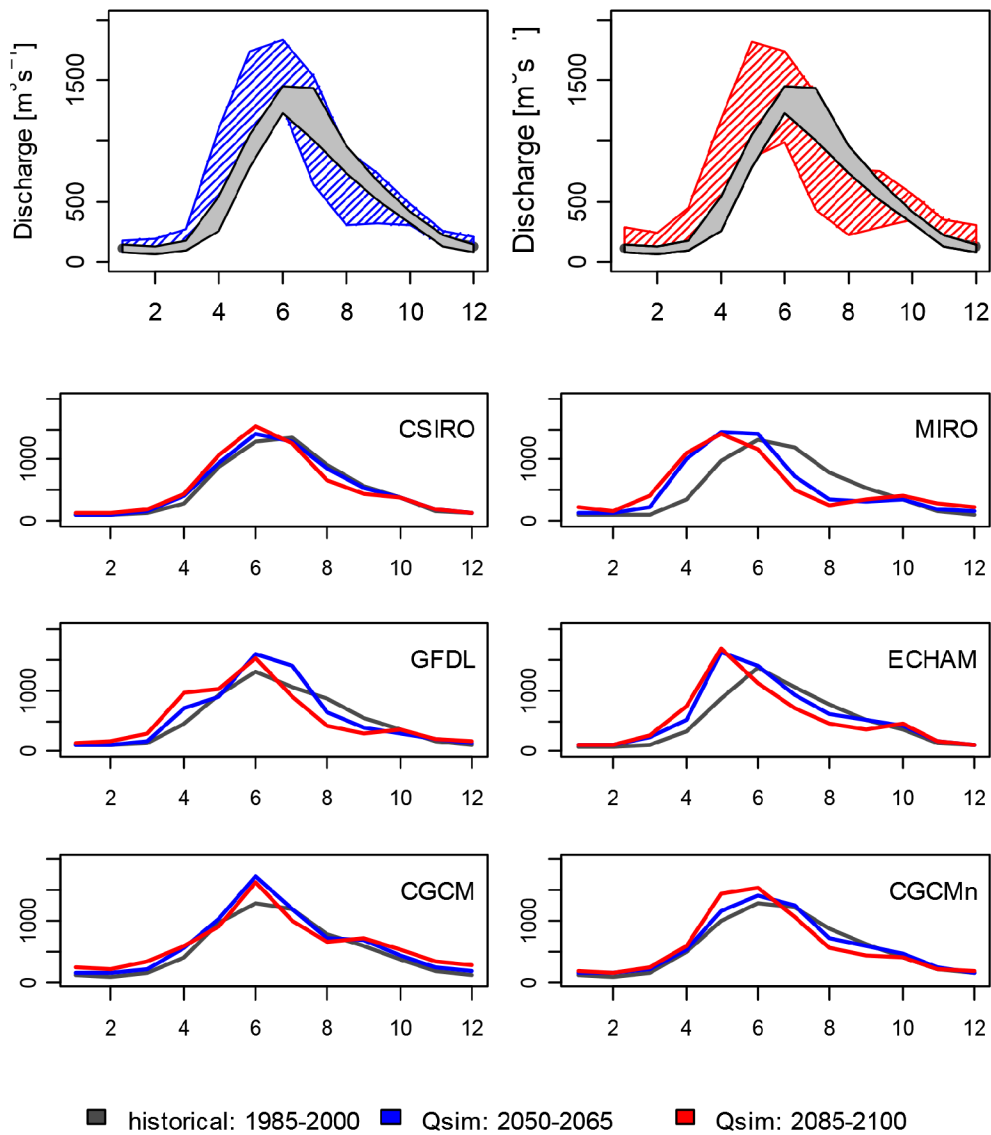


**Figure 7.10.** Projected seasonal streamflow response under the A1B scenario for 2050-2065 (blue) and 2085-2100 (red) time slices compared to historic baseline (black). Top: ensemble range for historic baseline runs (grey) compared to 2050-2065 time slice (top left) and compared to 2085-2100 time slice (top right) Bottom graphs: ensemble means (23 parameter sets) of 2050-2065 (blue) and 2085-2100 (red) time slices for each GCM.



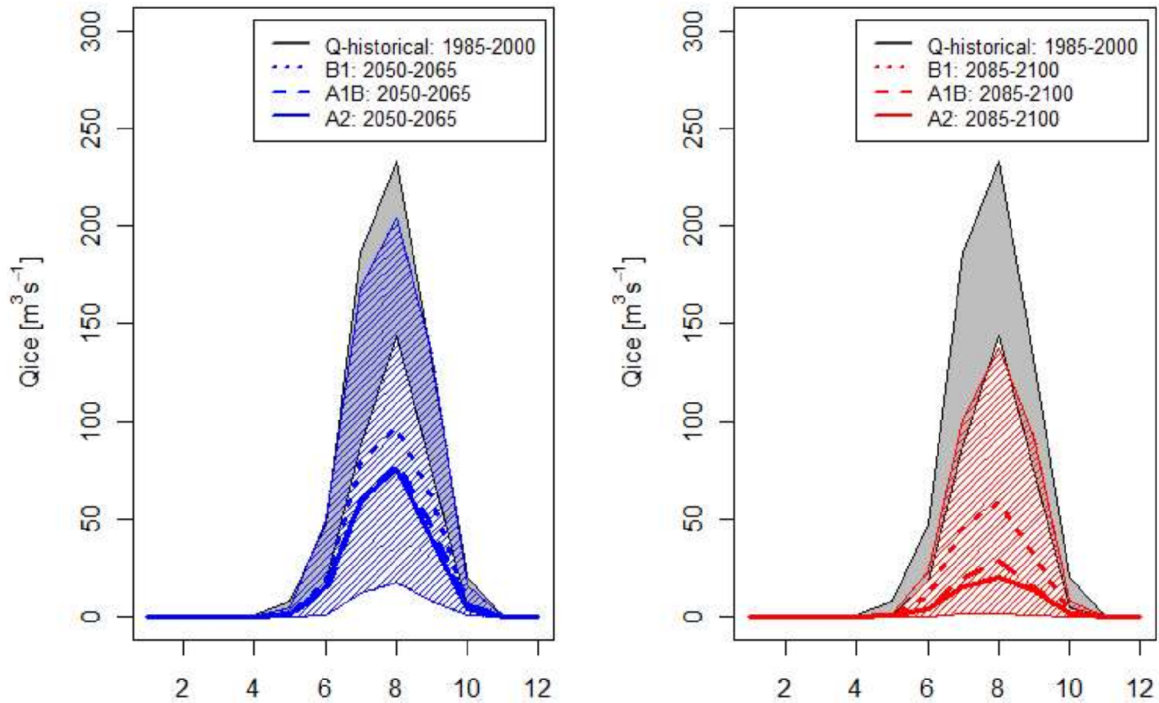


**Figure 7.11.** Historic and projected contribution of glacier ice melt ( $Q_{ice}$ ) for each month of the year for 2050-2065 (left) and 2085-2100 (right) time slices. The hashed areas (blue = 2050 -2065; red = 2085-2100) cover the range of uncertainties in GCM model selection, uncertainties in emission scenario selection, and uncertainties in parameter estimation for HBV-EC. Solid, dotted, and dashed lines show means for B1, A2, and A1B emission scenario over all GCMs (blue = 2050-2065; red = 2085-2100). The "historic" contributions, shown by black lines and grey shading, were modelled, not observed directly.

As pointed out in section 3, the contribution of glacier ice melt to annual streamflow during the historic period is relatively minor in most years compared to catchments with greater glacier cover. This is also true for future projections under all emission scenarios. However, with the decline of August streamflow in all projections due to an advanced snowmelt,  $Q_{ice}$  can become more important in the future for scenarios with enough glacier area persisting to produce significant quantities of ice melt. Hence, those scenarios and GCMs that project persistence of glacier cover in the future also project  $Q_{ice}$  to be more important in contributing to mean August streamflows.

For the 2050-2065 time slice under the B1 emission scenario, most GCMs project  $Q_{ice}$  to be a less important source of streamflow than in the historic period (Figure 7.12). At the end of the 21<sup>st</sup> century, all GCMs project a lower contribution of  $Q_{ice}$  to mean August streamflow than in the historic period. MIRO, GFDL and ECHAMS project the smallest contributions of  $Q_{ice}$  towards 2100, CSIRO the highest.

B1

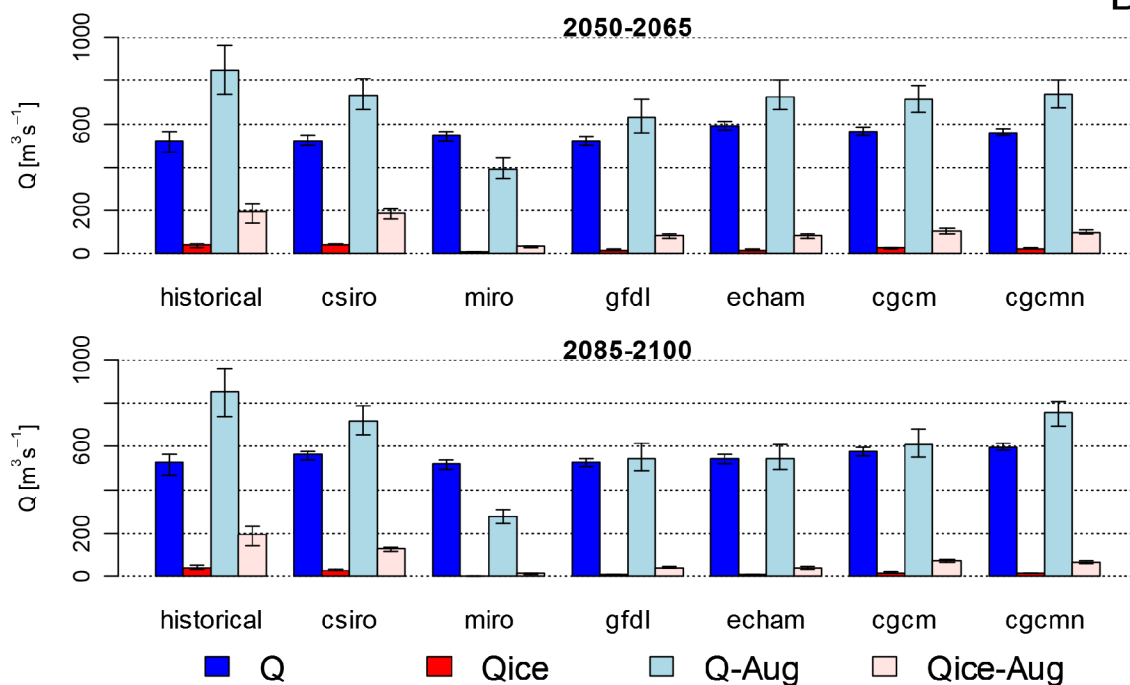


**Figure 7.12.** Historic and projected mean annual streamflow ( $Q$ ) with mean annual contribution of glacier ice melt ( $Q_{ice}$ ) and mean August streamflow ( $Q-Aug$ ), with mean August contribution of ice melt ( $Q_{ice-Aug}$ ) under emission scenario B1 for all GCMs. Error bars denote the upper and lower range of projections from 23 parameter sets.

Under the A2 emission scenario,  $Q_{ice}$  decreases to about a third of its historic baseline in the 2050-2065 time slice (Figure 7.13). The relative contribution of  $Q_{ice}$  to mean August flows decreases substantially in the 2085-2100 period for all GCMs, essentially disappearing in the scenario based on the GFDL GCM.

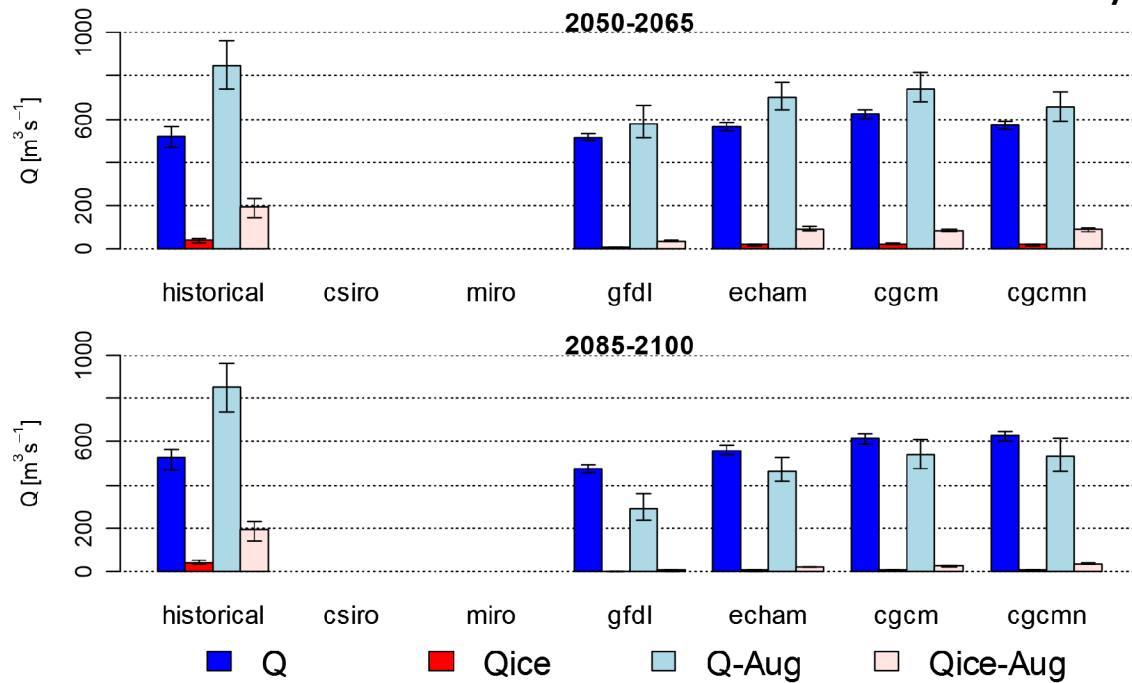


**Figure 7.13.** Historic and projected mean annual streamflow ( $Q$ ) with mean annual contribution of glacier ice melt ( $Q_{ice}$ ) and mean August streamflow ( $Q-Aug$ ), with mean August contribution of ice melt ( $Q_{ice-Aug}$ ) under emission scenario A2 for all GCMs. Error bars denote the upper and lower range of projections from 23 parameter sets.

In projections based on the A1B emission scenario,  $Q_{ice}$  is still a modest source of mean August streamflow in the 2050-2065 time slice, but decreases substantially towards the end of the 21<sup>st</sup> century (Figure 7.14). Projections based on MIRO and GFDL forcing indicate a negligible flow contribution from  $Q_{ice}$  due to the small amount of glacier coverage by the mid 21<sup>st</sup> century (Figure 6.5).

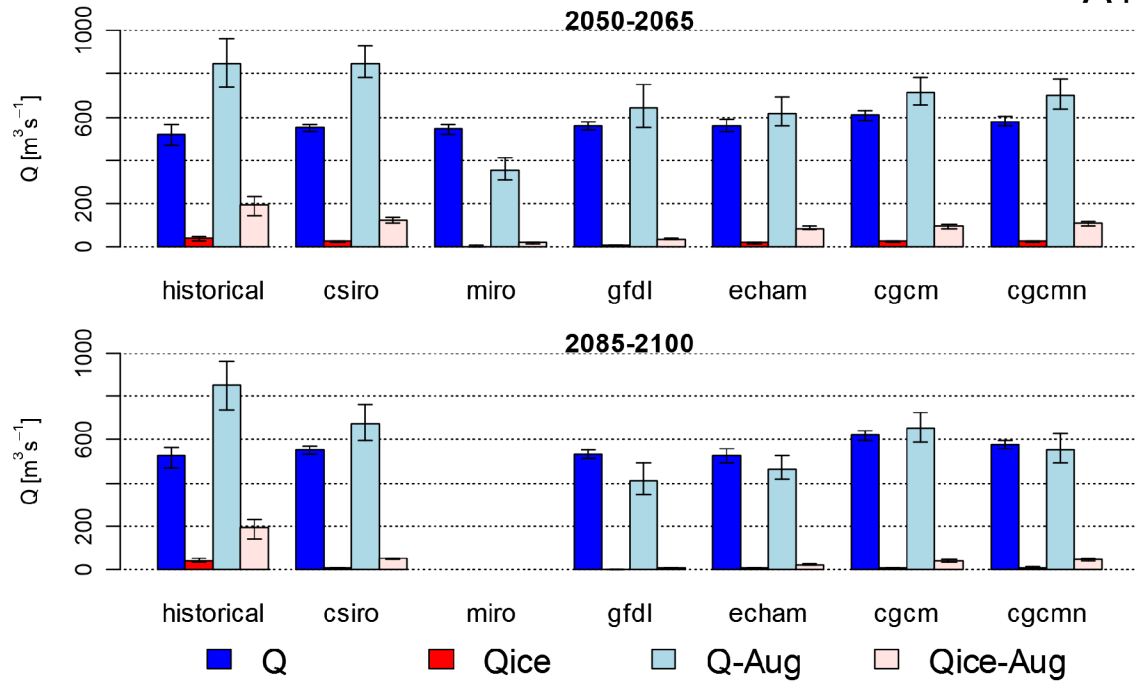


**Figure 7.14.** Historic and projected mean annual streamflow ( $Q$ ) with mean annual contribution of glacier ice melt ( $Q_{ice}$ ) and mean August streamflow ( $Q_{Aug}$ ), with mean August contribution of ice melt ( $Q_{ice-Aug}$ ) under emission scenario A1B for all GCMs. Error bars denote the upper and lower range of projections from 23 parameter sets.

## 8 Discussion

### 8.1 *Novel methodological contributions*

This study has made a number of pioneering contributions to the assessment of the hydrologic consequences of climate change in glacier-fed catchments. We would like to highlight the following:

1. It is the first study, to our knowledge, to use a physically based glacier dynamics model to make projections of the transient response of glaciers to future climate scenarios to provide boundary conditions for hydrologic modelling in a large catchment. Previous studies have used volume-area scaling (Stahl *et al.* 2008), adjustment of glacier thickness using a parameterized model (Huss *et al.* 2008), depletion of static glaciers with assumed thickness distributions (Rees and Collins 2006), adjustment of future glacier area based on a constant accumulation area ratio (Horton *et al.* 2006), or arbitrary assumptions about future decreases in glacier area for future time slices (e.g., Loukas *et al.* 2002; Hagg *et al.* 2006; Akhtar *et al.* 2008).
2. It is the first study to use changes in glacier volume and area to assist in hydrologic model calibration using a GLUE-type approach. This point is important given the lack of direct measurements of mass balance over most of the world's mountain regions, and especially in western Canada.
3. It is the first study in a glacier-fed catchment that has included a comprehensive assessment of uncertainties associated with uncertainties in hydrologic parameters, variation among emission scenarios and variation among GCMs.

In the process of conducting this study, we identified a number of challenges that would be appropriate targets for future research, as outlined in the next two sections.

### 8.2 *Hydrologic modelling with transient land cover*

HBV-EC, like many popular hydrologic model codes, treats land cover (and other boundary conditions such as soil characteristics) as static. Our approach to accommodating changes in glacier extent, although workable, involved substantial intervention in the model runs to update the glacier extents, with a significant increase in run time. Another drawback of the approach is the need to spin up the model each

time the glacier cover is updated. This further increases run time and, more fundamentally, increases the potential for simulation errors associated with the effects of incorrect initial conditions. As pointed out in section 3.3, using too long a spin-up time can produce errors in glacier-fed catchments under some circumstances, in addition to errors associated with using too short a spin-up time.

Stahl *et al.* (2008) dealt with this issue by recoding HBV-EC to include a glacier response model based on volume-area scaling, with rules for how to adjust state variables such as soil moisture when the land cover in a Grouped Response Unit changed from glacier to open or *vice versa*. While this solution overcame the problems of inefficiency and spin-up times, it is likely not optimal to code a physically based glacier dynamics model into a hydrologic model. Even if a glacier dynamics model were embedded into a hydrologic model, there is still the issue that other aspects of land cover can change (e.g., forest cover), with additional hydrologic consequences. In addition, given current computing technology, a hydrologic model with an embedded glacier dynamics model would run too slowly to allow the number of runs required to apply a GLUE-type approach for uncertainty assessment.

Our recommendation is to develop hydrologic models that can accommodate changes in land cover as part of a simulation run. Such a model would read in land cover descriptions at user-specified simulation time steps and update both the boundary conditions and the necessary state variables. In addition to addressing the issues associated with run-time efficiency and model spin-up, another important advantage of this approach is that state-of-the-art models of landscape change could be used without recoding the hydrologic model.

### **8.3 The validity of temperature-index melt models under future climate forcing**

Both the glaciation and hydrologic models use a temperature-index (TI) approach to simulate melt rates for snow and ice. While an energy balance (EB) approach is, in principle, superior to temperature-index approaches, it has been difficult to demonstrate any advantage of these models relative to temperature-index models in operational applications (Sorooshian *et al.* 2009). However, a compelling argument in favour of energy balance models for assessing the hydrologic impacts of climate change is that TI models rely on the correlations between air temperature and the various energy exchanges that drive snowmelt. In some cases, these linkages are direct (e.g., longwave radiation and sensible heat exchange are both directly controlled by air temperature) while others are indirect (e.g., air temperature tends to be high on sunny days, producing a positive correlation between air temperature and incident solar radiation). There

is no guarantee that these correlations would remain stable under changing climatic conditions, such that melt factors calibrated to current conditions may not be appropriate in the future.

While this argument is compelling, we believe that the advantages of energy balance models are, to a large extent, illusory. Even under current conditions, there is substantial uncertainty in parameters such as the albedo and its variation in time. For example, applications of the physically based snow routine in the Distributed Hydrology-Soil-Vegetation Model at three sites in British Columbia have required modification of the albedo parameterization based on local field data (Whitaker *et al.* 2003, Thyer *et al.* 2004, Jost *et al.* 2009), and there is no guarantee that parameterizations developed under current conditions will apply in the future. A further issue is that, as far as we are aware, all studies that have used GCM output to produce future climate scenarios only used downscaled air temperature and precipitation as model forcing (e.g., Loukas *et al.* 2002, Merritt *et al.* 2006), and the application of EB models using this type of climate forcing would have to rely on parameterizations of the energy fluxes as functions of air temperature and precipitation (following an approach similar to that advocated by Walter *et al.* 2005). Considering that the relations between, e.g., air temperature and incident solar radiation, may change under future climate conditions, the use of EB models forced by downscaled air temperature and precipitation is subject to the same criticism as TI models.

Further research is required to develop robust methods for simulating snow surface energy exchange using the information available in GCM output. Regional Climate Models (RCMs) are increasingly being used as a tool for dynamic downscaling from GCM output (e.g., Huss *et al.* 2008; Akhtar *et al.* 2009). Given their increased resolution relative to GCMs, it may be feasible to use RCM output such as solar radiation and atmospheric longwave radiation to drive EB models. This avenue deserves further research.



## 9 Summary

This study examined the effects of future climate scenarios on glacier coverage and streamflow in the Mica basin. Future scenarios were generated by downscaling output from six Global Climate Models (CGCM, CGCMn, MIRO, ECHAMS, CSIRO and GFDL) and three emission scenarios (B1, A1B, A2). All scenarios indicate continued warming to the year 2100. Depending on GCM and scenario, predicted air temperature increases by 2050 range from 1.1 to 3.7 °C (mean = 2.0 °C). Air temperature projections for the end of the 21<sup>st</sup> century range from 1.4 to 5.6 °C (mean = 3 °C). By 2050, precipitation in the area is projected to increase on average by 9%, with projections from individual combinations of GCMs and emission scenarios ranging from a 3% decrease to a 19% increase. By the end of the 21<sup>st</sup> century, precipitation in the area is projected to increase between 4 and 25% (mean = 13%), depending on the GCM and emission scenario. Glaciers in the Columbia River basin have been retreating for at least the last two decades, and are projected to continue retreating under all of the future climate scenarios. Depending on the GCM and emission scenario, glacier cover in 2100 is projected to decrease by 44% to 100% of the 2000 coverage, which represented about 6% of the catchment area.

The future warming is projected to generate an earlier onset of spring melt and lower flows in late summer and early autumn, consistent with other studies focused on climate change impacts on streamflow in snow-dominated catchments (e.g., Loukas *et al.* 2002, Merritt *et al.* 2006). Glacier ice melt currently contributes between 3 and 9% of annual runoff (6% on average). Ice melt contributions are more important in August and September, when they can reach up to 25% and 35% of monthly runoff, respectively. Ice melt contributions to annual runoff decline in all future scenarios. Ice melt contributions to August streamflow also decline under most future climate scenarios, although some increases are projected for the 2050-2065 time slice under the B2 emission scenario, for which glacier retreat is not as extreme as for other scenarios. The loss of ice melt contributions to August streamflow exacerbates the effect of an earlier snowmelt.

There is substantial uncertainty in the future projections, arising from (1) variations among GCMs, (2) variations among greenhouse gas emission scenarios, and (3) uncertainty in the calibrated parameters in the hydrologic model. However, even considering these uncertainties, the projections indicate that streamflow will increase in March and April and decrease in August and September regardless of the GCM and emission scenario selected.

## 10 References

- Akhtar M, Ahmad N, Booij MJ. 2008. The impact of climate change on the water resources of Hindukush–Karakorum–Himalaya region under different glacier coverage scenarios. *Journal of Hydrology* **355**: 148-163.
- Alley R *et al.* 2007. Summary for Policymakers. In *Climate change 2007: The Physical Science Basis*. Contribution of Working Group I to the Fourth Assessment of the Intergovernmental Panel on Climate Change, Solomon S *et al.* (eds). Cambridge University Press: Cambridge. U.K. pp. 1–18.
- Arnold NS, Willis IC, Sharp MJ, Richards KS, Lawson WJ. 1996. A distributed surface energy-balance model for a small valley glacier. I. Development and testing for Haut Glacier d'Arolla, Valais, Switzerland. *Journal of Glaciology* **42**: 77–89.
- Bahr, D. 1997. Global distributions of glacier properties: A stochastic scaling paradigm. *Water Resources Research* **33**: 1669–1679.
- Barstad I, Smith RB. 2005. Evaluation of an orographic precipitation model. *Journal of Hydrometeorology* **6**: 85–99.
- Beven K, Binley A. 1992. The future of distributed models: model calibration and uncertainty prediction. *Hydrological Processes* **6**: 279-298.
- Beven K, Freer J. 2001. Equifinality, data assimilation, and uncertainty estimation in mechanistic modelling of complex environmental systems using the GLUE methodology. *Journal of Hydrology* **249**: 11-29.
- Bolch T, Menounos B, and Wheate R. 2010. Landsat-based inventory of glaciers in western Canada, 1985–2005. *Remote Sensing of Environment* **114**: 127–137.
- Braithwaite RJ. 1981. On glacier energy balance, ablation, and air temperature. *Journal of Glaciology* **27**: 381–391.
- Braun LN, Aellen M. 1990. Modelling discharge of glacierized basins assisted by direct measurements of glacier mass balance. In *Hydrology in Mountainous Regions. I - Hydrological Measurements; the Water Cycle* (Proceedings of two Lausanne Symposia, August 1990). IAHS Publ. No. 193, 1990, pp. 99-106.
- Brekke LD, Dettinger MD, Maurer EP, Anderson M. 2008. Significance of model credibility in estimating climate projection distributions for regional hydroclimatological risk assessments. *Climatic Change* **89**: 371-394.
- Buishand TA, Brandsma T. 2001. Multisite simulation of daily precipitation and temperature in the Rhine basin by nearest-neighbor resampling. *Water Resources Research* **37**: 2761–2776.

- Canadian Hydraulics Centre, 2006. EnSim Hydrologic Reference Manual, National Research Council, Ottawa. 251 pp.
- Cannon AJ, Whitfield PH, Lord ER. 2002a. Synoptic map-pattern classification using recursive partitioning and principal component analysis. *Monthly Weather Review* **130**: 1187–1206.
- Cannon AJ, Whitfield PH, Lord ER. 2002b. Automated, supervised synoptic map-pattern classification using recursive partitioning trees. *in* Preprints, The 16th Conference on Probability and Statistics in the Atmospheric Sciences, American Meteorological Society, J210–J216.
- Cassano JJ, Uotila P, Lynch AH, Cassano EN. 2007. Predicted changes in synoptic forcing of net precipitation in large Arctic river basins during the 21st century. *Journal of Geophysical Research* **112**: G04S49. DOI:10.1029/2006JG000332.
- Christensen J H, Giorgi F, Rummukainen M. Weighting models based on several RCM specific metrics: Exploring the concept. Climate Change Scenario Workshop, Zurich, 2 March 2010.
- Clarke GKC, Berthier, E, Schoof CG, Jarosch AH. 2009. Neural networks applied to estimating subglacial topography and glacier volume. *Journal of Climate* **22**: 2146–2160.
- Coquard J, Duffy PB, Taylor KE. 2004. Present and future surface climate in the western U.S. as simulated by 15 global climate models. *Climate Dynamics* **23**: 455-472.
- Cunderlik, J. et al., 2010. Intercomparison Study of Process-Oriented Watershed Models, Richmond, BC. Fleming SW, Cunderlik J, Jenkinson W, Thiemann M, B, L., 2010. A ‘horse race’ intercomparison of process-oriented watershed models for operational river forecasting. Presented at the Canadian Water Resources Association Annual Conference, Vancouver, BC.
- Eaton, B.C. and Moore, R.D. 2010. Regional hydrology. Chapter 4 in: Pike, R.G., T.E. Redding, R.D. Moore, R.D. Winkler and K.D. Bladon (editors). 2010. Compendium of Forest Hydrology and Geomorphology in British Columbia. B.C. Ministry of Forests and Range, Forest Science Program, Victoria, B.C. and FORREX Forum for Research and Extension in Natural Resources, Kamloops, B.C. Land Management Handbook 66. pp. 85-110.
- Farr TG, *et al.* 2007. The Shuttle Radar Topography Mission. *Reviews of Geophysics* **45**: RG2004, doi:10.1029/2005RG000183.
- Finnis J, Cassano J, Holland M, Serreze M, Uotilla P. 2008. Synoptically Forced Hydroclimatology of Major Arctic Watersheds in General Circulation Models, Part 1: the Mackenzie River Basin. *International Journal of Climatology* **29**: 1226-1243.
- Fleming SW, Whitfield PH, Moore RD, Quilty EJ. 2007. Regime-dependent streamflow sensitivities to Pacific climate modes cross the Georgia-Puget transboundary ecoregion. *Hydrological Processes* **21**: 3264-3287.

- Fleming S, Cunderlik J, Jenkinson W, Thiemann M, Lence B. 2010. A 'horse race' intercomparison of process-oriented watershed models for operational river forecasting, Canadian Water Resources Association Annual Conference, Vancouver, BC, 2010.
- Freer J, Beven K, Ambrose B. 1996. Bayesian estimation of uncertainty in runoff prediction and the value of data: An application of the GLUE approach. *Water Resources Research* **32**: 2161-2173.
- Gleckler PJ, Taylor KE, Doutriaux C. 2008. Performance metrics for climate models. *Journal of Geophysical Research* **113**: DO6104. DOI: 10.1029/2007JD008972.
- Gray DM, Male DH. 1981. *Handbook of Snow: Principles, Processes, Management and Use*. New York: Pergamon Press.
- Gruber U, Bartlet P. 2007. Snow avalanche hazard modelling of large areas using shallow water numerical methods and GIS. *Environmental Modelling and Software* **2**: 1472–1481.
- Hagg W, Braun LN, Weber M, Becht M. 2006. Runoff modelling in glacierized Central Asian catchments for present-day and future climate. *Nordic Hydrology* **37**: 93– 105.
- Hamann A, Wang T. 2005. Models for climatic normals for geneecology and climate change studies in British Columbia. *Agricultural and Forest Meteorology* **128**: 211–221.
- Hamilton AS, Hutchinson DG, Moore RD. 2000. Estimating winter streamflow using conceptual streamflow model. *Journal of Cold Regions Engineering* **14**: 158-175.
- Hewitson B, Crane R. 2002. Self-organizing maps: Applications to synoptic climatology. *Climate Research* **22**: 13-26. DOI: 10.3354/cr022013.
- Hock R. 1999. A distributed temperature-index ice- and snowmelt model including potential direct solar radiation. *Journal of Glaciology* **45**: 101–111.
- Hoffman MJ, Fountain AG, Liston GE. 2008. Surface energy balance and melt thresholds over 11 years at Taylor Glacier, Antarctica. *Journal of Geophysical Research-Earth Surface* **113**: F04014, doi:10.1029/2008JF001029.
- Hofierka J, Suri M. 2002. The solar radiation model for open source GIS: implementation and applications. *Proceedings of the Open source GIS – GRASS users conference 2002*. Trento, Italy. 19 pp.
- Horton P, Schaefli B, Mezghani A, Hingray B, Musy A. 2006. Assessment of climate-change impacts on alpine discharge regimes with climate model uncertainty. *Hydrological Processes* **20**: 2091–2109.
- Houtekamer, P.L., Lefaiivre, L., Derome, J., Ritchie, H., Mitchell, H.L., 1996. A system simulation approach to ensemble prediction. *Monthly Weather Review* **124(6)**: 1225-1242.
- Huss M, Farinotti D, Bauder A, Funk M. 2008. Modelling runoff from highly glacierized alpine drainage basins in a changing climate. *Hydrological Processes* **22**: 3888–3902.

- Huth R. 2004. Sensitivity of local daily temperature change estimates to the selection of downscaling models and predictors. *Journal of Climate* **17**: 640–652.
- Huybers K, Roe G. 2009. Spatial patterns of glaciers in response to spatial patterns in regional climate, *Journal of Climate* **22**: 4606–4620.
- Imbert A, Benestad RE. 2005. An improvement of analog model strategy for more reliable local climate change scenarios. *Theoretical and Applied Climatology* **82**: 245–255.
- Jarosch AH, Anslow FS, Clarke GKC. 2010. High resolution precipitation and temperature downscaling for glacier models. *Climate Dynamics*, DOI: 10.1007/s00382-010-094901.
- Konz M, Seibert J. 2010. On the value of glacier mass balances for hydrological model calibration. *Journal of Hydrology* **385**: 238-246.
- Klok EJ, Oerlemans J. 2002. Model study of the spatial distribution of the energy balance of Morteratschgletscher, Switzerland. *Journal of Glaciology* **48**: 505–518.
- Kohonen T, Hynninen J, Kangas J, Laaksonen J. 1996. SOM\_PAK: The Self-Organizing Map Program Package. Technical Report A31; 27 pp. Helsinki University of Technology, Laboratory of Computer and Information Science, FIN-02150 Espoo, Finland.
- Kohonen T. 2000. *Self-Organizing Maps*. 3rd edition. Springer: New York; 528 pp.
- Konz M, Seibert J. 2010. On the value of glacier mass balances for hydrological model calibration. *Journal of Hydrology* **385**: 238-246.
- Krzysztofowicz, R., 1999. Bayesian theory of probabilistic forecasting via deterministic hydrologic model. *Water Resources Research* **35(9)**: 2739-2750.
- Krzysztofowicz, R., 2001. The case for probabilistic forecasting in hydrology. *Journal of Hydrology* **249(1-4)**: 2-9.
- Leduc M, Laprise R. 2010. Quantifying climate change signal and spread from an “ensemble of opportunity.” 44<sup>th</sup> Annual Canadian Meteorological and Oceanographic Society (CMOS) Congress, Ottawa, Canada.
- Lindstrom G, Johansson B, Persson M, Gardelin M, Bergström S. 1997. Development and test of the distributed HBV-96 hydrological model. *Journal of Hydrology* **201**: 272-288.
- Liston GE, Elder K. 2006. A meteorological distribution system for high-resolution terrestrial modeling (MicroMet). *Journal of Hydrometeorology* **7**: 217–234.
- Loukas A, Vasiladias L, Dalezios NR. 2002. Climatic impacts on the runoff generation processes in British Columbia, Canada. *Hydrology and Earth System Science* **6**: 211-227.
- Machguth H., Eisen O, Paul F, Hoelzle M. 2006. Strong spatial variability of snow accumulation observed with helicopter-borne GPR on two adjacent Alpine glaciers. *Geophysical Research Letters* **33**: L13503, doi:10.1029/2006GL02657

- Mantua NJ, Hare SR, Zhang Y, Wallace JM, Francis RC. 1997. A Pacific interdecadal climate oscillation with impacts on salmon production. *Bulletin of the American Meteorological Society* **78**:1069-1079.
- Marshall SJ, Tarasov L, Clarke GKC, Peltier WR. 2000. Glaciological reconstruction of the Laurentide Ice Sheet: physical processes and modelling challenges. *Canadian Journal of Earth Sciences* **37**: 769–793.
- Matulla C, Watson E, Wagner S, Schöner W. 2008. Downscaled GCM projections of winter and summer mass balance for Peyto Glacier, Alberta, Canada (2000-2100) from ensemble simulations with ECHAM5-MPIOM. *International Journal of Climatology* **29**: 1550 – 1559.
- Mebane WR, Sckhon JS. 2009. Genetic Optimization Using Derivatives : The rgenoud package for R. *Journal of Statistical Software*, Forthcoming. Available at: <http://www.jstatsoft.org/>.
- Merritt W, Alila Y, Barton M, Taylor B, Cohen S, Neilsen D. 2006. Hydrologic response to scenarios to climate change in sub watersheds of the Okanagan basin, British Columbia. *Journal of Hydrology* **326**: 79-108.
- Mesinger F, DiMego G, Kalnay E, Mitchell K, Shafran PC, Ebisuzaki W, Jovic D, Woollen J, Rogers E, Berbery EH, Ek MB, Fan Y, Grumbine R, Higgins W, Li H, Lin Y, Manikin G, Parrish D, Shi W. 2006. North American Regional Reanalysis. *Bulletin of the American Meteorological Society* **87**(3): 343–360.
- Mitchell TD, Jones PD. 2005. An improved method of constructing a database of monthly climate observations and associated high resolution grids. *International Journal of Climatology* **25**: 693–712.
- Moore RD. 1993. Application of a conceptual streamflow model in a glacierized drainage basin. *Journal of Hydrology* **150**: 151-168.
- Moore RD, Demuth MN. 2001. Mass balance and streamflow variability at Place Glacier, Canada, in relation to recent climate fluctuations. *Hydrological Processes* **15**: 3473-3486.
- Mote PW, Salathe EPJ. 2009. Future climate in the Pacific Northwest, Chapter 1: The Washington Climate Change Impacts Assessment. JISAO Climate Impacts Group, University of Washington, Seattle, WA, USA. pp. 21-43. <http://cscs.washington.edu/cig/res/ia/waccia.shtml>
- New M, Hulme M, Jones P. 2000. Representing twentieth-century space-time climate variability, Part II: Development of 1901-1996 monthly grids of terrestrial surface climate. *Journal of Climate* **13**: 2217–2238.
- Oerlemans J. 2005. Extracting a climate signal from 169 glacier records. *Science* **310**: 675-677.
- PCIC, Pacific Climate Impacts Consortium, Regional Analysis Tool, accessed March 24, 2010. <[www.pacificclimate.org/tools/regionalanalysis/](http://www.pacificclimate.org/tools/regionalanalysis/)>

- Pierce DW, Barnett TP, Santer BD, Gleckler PJ. 2009. Selecting global climate models for regional climate change studies. *Proceedings of the National Academy of Sciences* **106(21)**: 8441-8446.
- Pincus R, Batstone CP, Hofmann RJP, Taylor KE, Gleckler PJ. 2008. Evaluating the present-day simulation of clouds, precipitation, and radiation in climate model. *Journal of Geophysical Research* **113**: D14209. DOI: 10.1029/2007JD009334.
- R Development Core Team, 2009. R: A language and environment for statistical computing. Available at: <http://www.r-project.org>.
- Rasmussen, LA, Conway H. 2001. Estimating South Cascade Glacier (Washington, U.S.A.) mass balance from a distant radiosonde and comparison with Blue Glacier. *Journal of Glaciology* **47**: 579–588.
- Rasmussen, LA, Conway H. 2003. Using NCEP–NCAR Reanalysis data to estimate South Cascade Glacier (U.S.A.) summer balance. *Journal of Glaciology* **49**: 456–462.
- Rees HG , Collins DN. 2006. Regional differences in response of flow in glacier-fed Himalayan rivers to climatic warming. *Hydrological Processes* **20**: 2157–2169. DOI: 10.1002/hyp.6209.
- Schaeffli B, Hingray B, Niggli M, Musy A. 2005. A conceptual glacio-hydrological model for high mountainous catchments. *Hydrology and Earth System Sciences* **9**: 95-109.
- Schiefer E, Menounos B, and Wheate R. 2007. Recent volume loss of British Columbian glaciers, Canada, *Geophysical Research Letters* **34**: L16503, doi:10.1029/2007GL030780.
- Schuenemann KC, Cassano JJ. 2009. Changes in synoptic weather patterns and Greenland precipitation in the 20th and 21st centuries: 1. Evaluation of late 20th century simulations from IPCC models. *Journal of Geophysical Research* **114**: D20113. DOI: 10.1029/2009JD011705.
- Seibert J, Beven K. 2009. Gauging the ungauged basin: how many discharge measurements are needed? *Hydrology and Earth System Sciences* **6**: 2275-2299.
- Smith RB, Barstad I. 2004. A linear theory of orographic precipitation. *Journal of the Atmospheric Sciences* **61**: 1377–1391.
- Smith RB. 2003. A linear upslope-time-delay model for orographic precipitation. *Journal of Hydrology* **282**: 2–9.
- Stahl K, Moore RD, McKendry IG. 2006. The role of synoptic-scale circulation in the linkage between large-scale ocean-atmosphere indices and winter surface climates in British Columbia, Canada. *International Journal of Climatology* **26**: 541-560.
- Stahl K, Moore RD, Shea JM, Hutchinson DG, Cannon A. 2008. Coupled modelling of glacier and streamflow response to future climate scenarios. *Water Resources Research* **44**, W02422, doi:10.1029/2007WR005956.
- Stenborg T. 1970. Delay of runoff from a glacier basin. *Geografiska Annaler* **52A**: 1-30.



- Thyer M, Beckers J, Spittlehouse D, Alila Y, Winkler R. 2004. Diagnosing a distributed hydrologic model for two high-elevation forested catchments based on detailed stand- and basin-scale data. *Water Resources Research* **40**: doi:10.1029/2003WR002414, 2004.
- Walter MT , Brooks ES, McCool DK, King LG, Molnau M, Boll J. 2005. Process-based snowmelt modeling: Does it require more input data than temperature-index modeling? *Journal of Hydrology* **300**: 65-75.
- Wang T, Hamann A, Spittlehouse D, Aitken S. 2006. Development of scale-free climate data for Western Canada for use in resource management. *International Journal of Climatology* **26**: 383–397.
- Whitaker A, Alila Y, Beckers J, Toews D. 2003. Application of the distributed hydrology soil vegetation model to Redfish Creek, British Columbia: model evaluation using internal catchment data. *Hydrological Processes* **17**: 199-224.

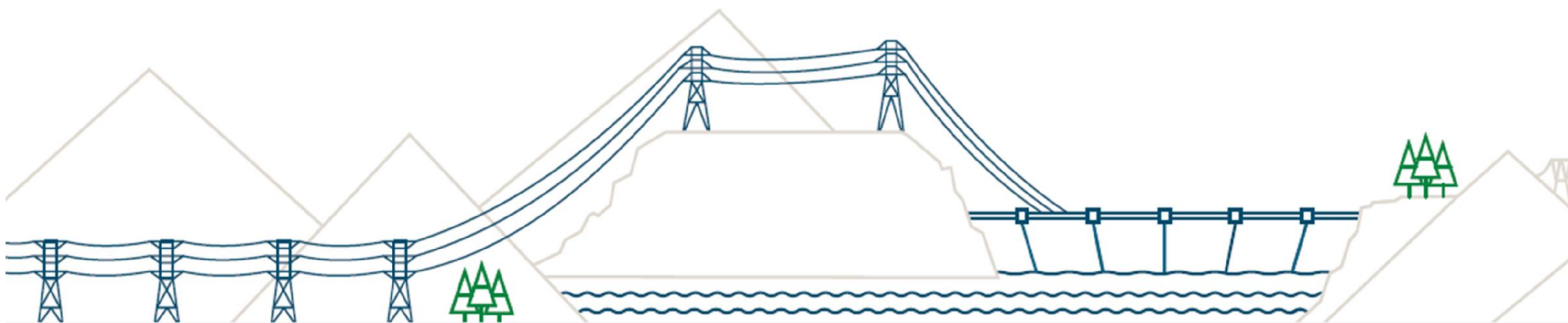
# Water Year 2017 – BC Hydro

Scott Weston

Adam Gobena

Georg Jost

Stephanie Smith



2017-12-04

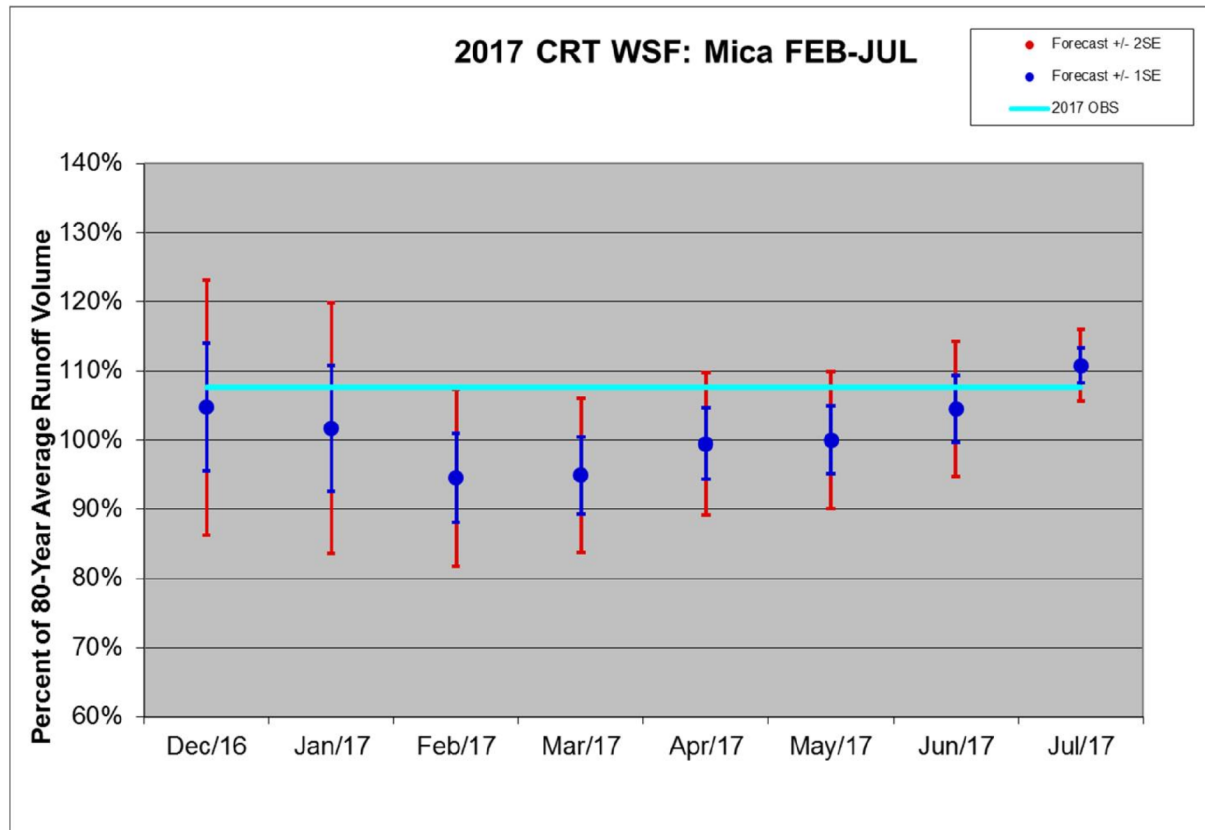
 **BC Hydro**  
Power smart

# Water Year 2017

Scott Weston did all the work



# Mica – prediction uncertainty



# Started with heavy rain in fall 2016

